J. Fluid Mech. (2011), *vol.* 671, *pp.* 507–534. © Cambridge University Press 2011
doi:10.1017/S002211201000580X

Large-eddy simulations of turbulent mixing layers using the stretched-vortex model

T. W. MATTNER†

School of Mathematical Sciences, The University of Adelaide, SA 5005, Australia

(Received 6 May 2009; revised 20 October 2010; accepted 7 November 2010;
first published online 11 February 2011)

The stretched-vortex subgrid model is used to run large-eddy simulations of temporal mixing layers at various Reynolds and Schmidt numbers, with different initial and boundary conditions. A self-similar flow is obtained, during which the growth rate, mean velocity and Reynolds stresses are in accord with experimental results. However, predictions of the amount of mixed fluid, and of the variation in its composition across the layer, are excessive, especially at high Schmidt number. More favourable comparisons between experiment and simulation are obtained when the large-scale flow is quasi-two-dimensional; however, such states are not self-similar and not sustainable. Present model assumptions lead to predictions of the continued subgrid spectrum with a viscous cutoff that is dependent on grid resolution.

Key words: shear layer turbulence, turbulence simulation, turbulent mixing

1. Introduction

Turbulent flows are characterised by irregular unsteady three-dimensional fluid motion over a wide range of spatial and temporal scales. Prediction of many turbulent flows by direct numerical simulation remains impracticable due to the enormous computational resources needed to resolve all relevant scales. This problem is mitigated in a large-eddy simulation because only the large-scale features of the flow are resolved, while the fine-scale subgrid features are modelled. Many subgrid models have been developed, some of which are described by Lesieur & Metais (1996) and Meneveau & Katz (2000). In the present study, the stretched-vortex model developed by Pullin and coworkers has been used to simulate high-Reynolds-number incompressible temporal mixing layers, with particular emphasis on subgrid statistics and passive scalar mixing.

The stretched-vortex model has been applied to a variety of flows, including incompressible and compressible isotropic homogeneous turbulence (Misra & Pullin 1997; Kosovic, Pullin & Samtaney 2002), rotating and nonrotating channel flows (Voekl, Pullin & Chan 2000; Pantano *et al.* 2008; Chung & Pullin 2009), incompressible Rayleigh–Taylor instability (Mattner, Pullin & Dimotakis 2004), trailing vortices (Faddy & Pullin 2005) and compressible Richtmyer–Meshkov instability (Hill, Pantano & Pullin 2006). In Hill *et al.* (2006), methods for estimating the subgrid-scale spectra of the velocity and scalar fields, as well as the probability density function (p.d.f.) of the scalar field, were developed. However, owing to the paucity of suitable experimental data for the flow, some of these predictions could not be directly verified.

† Email address for correspondence: trent.mattner@adelaide.edu.au

https://doi.org/10.1017/S002211201000580X Published online by Cambridge University Press

Mixing layers form between two parallel streams of fluid with different velocities. In experiments, mixing layers are usually produced by merging two streams which are initially separated by a plate. The flow that develops downstream of the trailing edge of the plate is a spatial mixing layer. Such flows have been studied extensively because of their technological significance in aerodynamics, combustion and chemical mixing, and because they are of intrinsic interest as a canonical turbulent shear flow. Temporal mixing layers form when the streams move at the same speed but in opposite directions and are often the subject of numerical simulations because the flow is homogeneous in both the streamwise and spanwise directions (Rogers & Moser 1994; Ansari 1997; Vreman, Geurts & Kuerten 1997; Balaras, Piomelli & Wallace 2001). Although the spatial and temporal flows are different, useful comparisons are still possible if the velocity ratio of the two streams of the spatial mixing layer is not too small (Rogers & Moser 1994).

It is often observed that the mixing layer becomes self-similar after sufficient development in space or time. Self-similarity is characterised by linear growth of the mixing-layer thickness with respect to space or time and invariance of statistics when scaled with the velocity difference across the layer and the mixing-layer thickness. However, the final self-similar state is not unique, depending on inlet boundary conditions such as the initial state of the plate boundary layers (Slessor, Bond & Dimotakis 1998) or initial conditions (Rogers & Moser 1994; Balaras *et al.* 2001). This means that even if a self-similar state is attained in a simulation, it need not be the same as that found in an experiment, unless the initial or inlet conditions are matched (as done by Druault *et al.* 2004). The implication for large-eddy simulation is even more serious because the characteristic length scales of the initial conditions are likely to be subgrid.

The distribution and composition of molecularly mixed fluid in a turbulent flow is important in many contexts. In combustion, for example, the amount of molecularly mixed fluid determines the amount of product formed and the heat released. Such mixing occurs at the finest scales of the flow. In experiments, it is often impossible to directly resolve a passive scalar convected in a turbulent flow, leading to erroneous estimates of the scalar p.d.f. Instead, experimentalists rely on chemical reactions (Koochesfahani & Dimotakis 1986; Karasso & Mungal 1996) or dual tracer techniques (Meyer, Dutton & Lucht 2006) to obtain resolution-free estimates of these statistics. The difference between the under-resolved and resolution-free data can be substantial, especially at high Schmidt number. A similar situation is encountered in large-eddy simulations because the subgrid scalar field is not directly available. It is impossible to tell from a local value of the filtered scalar field whether the subgrid scalar field is composed of mixed or unmixed fluid. The subgrid scalar model developed by Hill *et al.* (2006) specifically addresses this ambiguity.

While molecular mixing is a fine-scale process, the large-scale flow structure controls the entrainment and stirring processes, which in turn feeds the molecular mixing process (Dimotakis 1991). Rogers & Moser (1994) show that by promoting two-dimensional spanwise eddies or 'rollers' in a temporal mixing layer, the scalar p.d.f. changes from a 'marching' type, in which the most probable mixed-fluid composition varies across the layer, to a 'non-marching' type, in which the most probable mixed-fluid composition is nearly constant across the layer. Furthermore, they suggest that the large-scale structure associated with each type of scalar p.d.f. corresponds to distinct self-similar states. Variations in the scalar p.d.f. are often attributed to changes in the large-scale structure brought about by initial or inlet boundary conditions (e.g. Karasso & Mungal 1996; Slessor *et al.* 1998), other things being equal.

https://doi.org/10.1017/S002211201000580X Published online by Cambridge University Press

The aim of the present study is to use the stretched-vortex model, including the extensions developed by Hill *et al.* (2006), to simulate high-Reynolds-number temporal mixing layers and to compare those predictions with experimental data. The stretched-vortex subgrid model and the simulations are described in § 2. Apart from a minor difference in the model subgrid scalar spectrum and the addition of subgrid contributions to the resolved-scale one-dimensional spectrum, the model is the same as that proposed by Hill *et al.* (2006). The simulations are run at Reynolds numbers comparable with those of high-Reynolds-number experiments and at Schmidt numbers typical of gas and liquid-phase fluids. High Reynolds numbers are needed so that the subgrid model can dominate viscous or diffusive dissipation without accounting for excessive proportions of kinetic energy or scalar variance, and, together with a large domain, to encourage the development of self-similar flow. The simulations explore the effects of grid resolution, Reynolds and Schmidt numbers, initial conditions and boundary constraints.

Velocity statistics are presented in § 3. A self-similar state of flow is achieved, during which the mean velocity, Reynolds stress and growth rate compare favourably with experimental data (§ 3.1). Estimates of the total turbulent kinetic energy, energy dissipation, growth rate and Reynolds stress are not sensitive to grid resolution. However, the wavenumber of the viscous cutoff of the subgrid-continued spectra is found to be dependent on grid resolution (§ 3.2). The effect on integrated quantities is minimal because the subgrid contribution is typically small. Chung (2009) has developed methods to compensate for this grid-resolution effect, but these have not been implemented in this paper.

Scalar statistics are presented in § 4. For the self-similar flow, there are significant differences between the mixed-fluid statistics derived from the scalar p.d.f. of the simulations and those obtained from fully resolved measurements, especially at high Schmidt number. However, it is found that the same statistics compare favourably with under-resolved measurements, which supports the conjecture that the large-scale structure of the scalar field predicted by the simulations is consistent with that of the experiment (§ 4.1) and that the present subgrid model overestimates the degree of mixing. Estimates of the total turbulent scalar energy and the scalar dissipation are more sensitive to grid resolution than the analogous quantities from the velocity field, as are the subgrid-continued scalar spectra (§ 4.2).

In § 4.3, the effect of initial conditions and boundary constraints on the flow structure and the resulting mixed-fluid statistics is examined. It is found that model predictions of mixed-fluid statistics are more consistent with experimental data when the large-scale flow is quasi-two-dimensional, in accordance with Rogers & Moser (1994). However, the degree of two-dimensionality needed to produce the necessary effect is strong. Furthermore, when initial conditions are used to induce such a state, self-similarity is not achieved and the flow eventually evolves to a state of mixing that is essentially the same as that of the self-similar layer described in § 4.1.

2. Problem formulation and computational methods

2.1. *Governing equations*

Consider passive scalar mixing by an incompressible flow. The equations of motion for large-eddy simulation are

$$\frac{\partial \overline{u}_j}{\partial x_j} = 0, \tag{2.1a}$$

https://doi.org/10.1017/S002211201000580X Published online by Cambridge University Press

$$\frac{\partial \overline{c}}{\partial t} + \frac{\partial \overline{u}_j \overline{c}}{\partial x_j} = \frac{\partial}{\partial x_j}\left(\mathscr{D}\frac{\partial \overline{c}}{\partial x_j}\right) - \frac{\partial q_j}{\partial x_j}, \tag{2.1b}$$

$$\frac{\partial \overline{u}_i}{\partial t} + \frac{\partial \overline{u}_i \overline{u}_j}{\partial x_j} = -\frac{\partial \overline{p}/\rho}{\partial x_i} + \frac{\partial \overline{\tau}_{ij}}{\partial x_j} - \frac{\partial T_{ij}}{\partial x_j}, \tag{2.1c}$$

where x_i and u_i are the components of the Eulerian position and velocity vectors, respectively, c is the scalar concentration, $\mathscr{D}$ is the diffusivity, p is the pressure, τ_{ij} is the viscous stress tensor given by

$$\tau_{ij} = \nu\left[\frac{\partial u_i}{\partial x_j} + \frac{\partial u_j}{\partial x_i}\right], \tag{2.2}$$

and ν is the kinematic viscosity. In the model equations, overbars denote filtered variables

$$\overline{f} = \int G(\boldsymbol{x} - \boldsymbol{x}') f(\boldsymbol{x}')\,\mathrm{d}\boldsymbol{x}', \tag{2.3}$$

where G is a filter kernel. The additional terms,

$$q_j = \overline{u_j c} - \overline{u}_j \overline{c}, \tag{2.4}$$

and

$$T_{ij} = \overline{u_i u_j} - \overline{u}_i \overline{u}_j, \tag{2.5}$$

are the subgrid scalar flux and the subgrid stress, respectively.

The stretched-vortex subgrid stress model of Misra & Pullin (1997) and the stretched-vortex subgrid scalar flux model of Pullin (2000) are used to close (2.1b) and (2.1c). The subgrid stress is

$$T_{ij} = K\left(\delta_{ij} - e_i^v e_j^v\right), \tag{2.6}$$

where K is the subgrid kinetic energy per unit mass, and e_i^v are the components of a unit vector which is aligned with the subgrid vortex axis. The subgrid scalar flux is

$$q_j = -\frac{1}{2}\Delta K^{1/2}\left(\delta_{ij} - e_i^v e_j^v\right)\frac{\partial \overline{c}}{\partial x_i}, \tag{2.7}$$

where Δ is the local mesh size. The subgrid kinetic energy is

$$K = \int_{k_c}^{\infty} E(k)\,\mathrm{d}k, \tag{2.8}$$

where k is the wavenumber, $k_c = \pi/\Delta$ is the cutoff wavenumber, $E(k)$ is the spectrum of the Lundgren spiral vortex,

$$E(k) = \mathscr{K}_0 \epsilon^{2/3} k^{-5/3} \exp\left(-\frac{2k^2\nu}{3|a|}\right), \tag{2.9}$$

$\mathscr{K}_0$ is the Kolmogorov prefactor, ϵ is the local cell-averaged dissipation rate, $a = e_i e_j \overline{S}_{ij}$ is the axial strain along the subgrid vortex axis (Voekl *et al.* 2000) and $\overline{S}_{ij}$ is the resolved rate-of-strain tensor. The group $\mathscr{K}_0\epsilon^{2/3}$ is calculated from the local resolved spherically averaged second-order velocity structure function $\overline{F}_2$ using

$$\mathscr{K}_0 \epsilon^{2/3} = \frac{\overline{F}_2}{A\Delta^{2/3}}, \tag{2.10}$$

where $A = 4\int_0^{\pi} u^{-5/3}\,(1 - (\sin u/u))\,\mathrm{d}u \approx 1.90695$ (Lesieur & Metais 1996; Pullin 2000; Voekl *et al.* 2000). The resolved-scale structure function is estimated at the point $\boldsymbol{x}$

https://doi.org/10.1017/S002211201000580X Published online by Cambridge University Press

using

$$\overline{F}_2 = \frac{1}{6}\sum_{j=1}^{3}\left(\delta\overline{u}_1^{+2} + \delta\overline{u}_2^{+2} + \delta\overline{u}_3^{+2} + \delta\overline{u}_1^{-2} + \delta\overline{u}_2^{-2} + \delta\overline{u}_3^{-2}\right)_j, \tag{2.11}$$

where $\delta\overline{u}_i^{\pm} = \overline{u}_i(\boldsymbol{x} \pm \boldsymbol{e}_j\Delta) - \overline{u}_i(\boldsymbol{x})$ and $\boldsymbol{e}_j$ is the unit vector in the jth direction (Hill *et al.* 2006). Subgrid vortices are assumed to align either with the principal extensional eigenvector of the resolved rate-of-strain tensor, $\overline{S}_{ij}$, or with the resolved vorticity vector $\boldsymbol{\omega}$. The respective proportions are given by λ and $(1-\lambda)$, where

$$\lambda = \frac{\lambda_3}{\lambda_3 + \|\boldsymbol{\omega}\|} \tag{2.12}$$

and λ_3 is the principal extensional eigenvalue (Kosovic *et al.* 2002).

2.2. *Flow conditions*

The flow domain is a rectangular prism. Cartesian coordinates (x, y, z) are oriented in the streamwise, cross-stream and spanwise directions, respectively. The corresponding components of velocity are (u, v, w). Periodic boundary conditions are imposed in the homogeneous streamwise and spanwise directions. The top and bottom of the domain are modelled as free-slip walls, as in earlier simulations by Vreman *et al.* (1997). This is satisfactory if the mixing-layer thickness is much smaller than the domain size. In other mixing-layer simulations, wall effects are either eliminated by using a domain with an infinite cross-stream extent (Rogers & Moser 1994; Ansari 1997) or minimised by applying radiation boundary conditions at the top and bottom walls (Balaras *et al.* 2001). Preliminary simulations showed that doubling the cross-stream extent of the domain changed the mixing-zone thickness by less than 1 %, even when it occupied 60 % of the original domain; hence, more sophisticated boundary conditions were considered unnecessary. Finite boundaries of any sort inevitably exert an influence on the flow (Balaras *et al.* 2001) and this will limit the duration of any self-similar regime of mixing-layer growth.

The initial mean velocity profile is

$$\frac{\overline{u}}{\Delta U} = \frac{1}{2}\tanh\left(\frac{y}{d}\right), \tag{2.13}$$

where ΔU is the velocity difference across the layer and d is set to approximately 1.6Δ (this is the thinnest resolvable on the grid). This is perturbed by a random, three-dimensional, divergence-free disturbance. The perturbation is created from random, three-dimensional, homogeneous seed disturbances with spectra of the form

$$\exp\left[-\left(\frac{k-k_0}{2\sigma}\right)^2\right], \tag{2.14}$$

where k_0 is the wavenumber of peak energy and σ is the width of the energy distribution. Anisotropic perturbations are obtained by setting $k = \sqrt{c_i^2 k_i^2}$, where k_i are the components of the wave vector and the relative values of the coefficients c_i control the degree of anisotropy. The seed perturbations are confined to the initial mixing layer by modulating them by

$$1 - \tanh^2\left(\frac{y}{d}\right). \tag{2.15}$$

https://doi.org/10.1017/S002211201000580X Published online by Cambridge University Press

Case	Domain size	L/Δ	Re_0	Re_{1200}	Sc	k_0/α	k_0/σ
1A	$2L \times L \times L$	256	800	14 400	1000	5	29
1B	$2L \times L \times L$	128	800	14 400	1000	–	–
1C	$2L \times L \times L$	64	800	14 400	1000	–	–
1D	$2L \times L \times L$	256	800	14 400	1	5	29
2A	$2L \times L \times L$	256	80 000	153 600	1000	5	29
2B	$2L \times L \times L$	128	80 000	153 600	1000	–	–
2C	$2L \times L \times L$	64	80 000	153 600	1000	–	–
3	$2L \times L \times L$	256	800	14 100	1000	5	29
4	$2L \times L \times L$	256	800	19 800	1000	1	28
5	$2L \times L \times L/8$	256	800	13 500	1000	5	29

TABLE 1. Simulation parameters. Cases 1B and 1C are initialised from case 1A, and cases 2B and 2C are initialised from case 2A.

The final velocity perturbation is obtained by projecting the seed velocity perturbation onto a divergence-free vector field. The initial scalar field is

$$\overline{c} = \frac{1}{2}\left[1 + \tanh\left(\frac{y}{d}\right)\right], \tag{2.16}$$

which is unperturbed.

High-resolution numerical schemes are needed in large-eddy simulations so that numerical errors do not overwhelm the subgrid stresses (Ghosal 1996). In the present simulations, standard high-order numerical schemes are used, but alternatives are available (Hill & Pullin 2004). A Fourier spectral collocation scheme is used in the homogeneous x- and z-directions. An eighth-order compact finite-difference scheme (Lele 1992) is used in the inhomogeneous y-direction. Aliasing is minimised by calculating the nonlinear convective terms in skew-symmetric form (Blaisdell, Spyropoulos & Qin 1996; Kravchenko & Moin 1997). A third-order variable-time-step Adams–Bashforth–Moulton scheme is used for temporal integration. The code implementing these methods was verified by running simulations of the incompressible unsteady Stuart vortex (Stuart 1967) and comparing these with the exact solution. The test simulations were run with the subgrid model turned off and boundary conditions derived from the exact solution.

Table 1 lists the parameters used for each simulation. The cross-stream dimension of the flow domain is denoted by L and is the same in each simulation. The grid spacing Δ is identical in each direction. The thickness of the mixing layer is characterised by the momentum thickness defined by

$$\theta = \int_{-\infty}^{\infty} \left[\frac{1}{4} - \left(\frac{\langle\overline{u}\rangle}{\Delta U}\right)^2\right] \mathrm{d}y, \tag{2.17}$$

where the angled brackets denote the plane average

$$\langle f\rangle(y) = \frac{1}{A}\iint_A f(x, y, z)\,\mathrm{d}z\,\mathrm{d}x, \tag{2.18}$$

where A is the area. In each case, the initial conditions give $L/\theta_0 = 320$, where θ_0 is the initial momentum thickness. For the initial hyperbolic-tangent velocity profile, linear stability theory (Michalke 1964) predicts that $\alpha \approx 0.22/\theta_0$, where α is the wavenumber of the most unstable mode. The streamwise dimension of the flow domain is $2L$, which is equivalent to approximately 22 wavelengths of the most unstable mode. The

https://doi.org/10.1017/S002211201000580X Published online by Cambridge University Press

aspect ratio of the domain is the same for each simulation except case 5. The default aspect ratio is motivated by measurements that show that the dominant spanwise length scale is about two thirds of the dominant streamwise length scale (Huang & Ho 1990). In case 5, the spanwise dimension of the flow domain is reduced by a factor of eight.

The Reynolds number listed in table 1 is

$$Re = \frac{\Delta U \theta}{\nu} \tag{2.19}$$

and the Schimdt number is

$$Sc = \frac{\nu}{\mathscr{D}}. \tag{2.20}$$

Two alternative definitions of the Reynolds number that appear frequently in the literature are $Re_h = \Delta U h/\nu$ and $Re_\delta = \Delta U \delta/\nu$, where h is the vorticity thickness and δ is the scalar mixing-zone thickness. The vorticity thickness is defined by $h = \Delta U/(\partial \overline{u}/\partial y)_{max}$, while the scalar mixing-zone thickness is defined by $\delta = y_{0.99} - y_{0.01}$, where $\langle \overline{c} \rangle (y_{0.99}) = 0.99$ and $\langle \overline{c} \rangle (y_{0.01}) = 0.01$. From the simulations, it is found that $h \approx 4.4\,\theta_0$ and $\delta \approx 8\,\theta_0$.

The initial Reynolds number Re_0 is the same for all simulations except cases A–C. The default value of $Re_0 = 800$ is the same initial Reynolds number as the direct numerical simulations of Rogers & Moser (1994). Note that Re_{1200} is the Reynolds number at the non-dimensional time $t/\tau = 1200$, where $\tau = \theta_0/\Delta U$. In the simulations that achieve self-similarity, Re_{1200} is an indication of the maximum Reynolds number achieved while the flow remains self-similar. For simulations that start at $Re_0 = 800$, Re_{1200} is approximately 14 000. This corresponds to $Re_h \approx 62\,000$ or $Re_\delta \approx 112\,000$. This range of Reynolds numbers spans those of previous direct numerical simulations of mixing layers (Rogers & Moser 1994; Ansari 1997) as well as many high-Reynolds-number experiments (Mungal & Dimotakis 1984; Koochesfahani & Dimotakis 1986; Bell & Mehta 1990; Karasso & Mungal 1996; Slessor *et al.* 1998).

The series of simulations listed in table 1 explore the effects of Reynolds number (case 2A), Schmidt number (case 1D), resolution (cases 1B, 1C, 2B and 2C) and flow structure (cases 3–5). Resolution effects are studied by repeating simulations on a coarse grid. Cases 1B and 1C are coarse-grid simulations of case 1A, while cases 2B and 2C are coarse-grid simulations of case 2A. These simulations are initialised by filtering data from the fine-grid simulation and interpolating them onto the coarse grid. Sharp spectral filters are used in the homogeneous x- and z-directions and a compact filter (Lele 1992, equation C.2.8) is used in the inhomogeneous y-direction. The coarse-grid simulations start at $t/\tau = 640$. For case 1C, this ensures that 80 % of the kinetic energy is resolved.

Various initial and boundary constraints were used to alter the flow structure. For cases 1A, 1D, 2A and 5, the initial perturbation is nearly isotropic in the x–z plane, with a dominant wavenumber k_0 that is five times larger than that of the most unstable mode α (figure 1*a*). For cases 3 and 4, the perturbation is elongated by a factor of four in the spanwise direction, giving a more two-dimensional disturbance. In case 3, the dominant wavenumber is the same as that of the default disturbance (figure 1*b*). In case 4, the dominant wavenumber is matched to that of the most unstable mode (figure 1*c*). In case 5, the spanwise dimension of the flow domain is significantly reduced in order to promote quasi-two-dimensional flow.

https://doi.org/10.1017/S002211201000580X Published online by Cambridge University Press

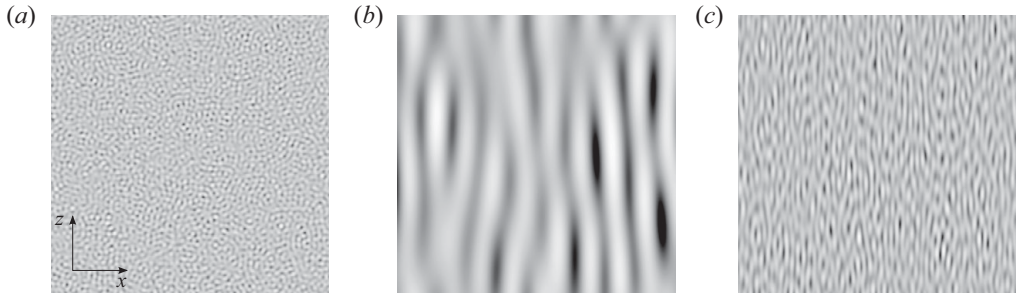


FIGURE 1. Spatial variation of the cross-stream velocity v at the midplane from (a) cases 1A, 1D and 2A; (b) case 3 and (c) case 4. Light and dark indicates maximum and minimum cross-stream velocity over the plane, respectively. The perturbation energy $\langle u_i'^2\rangle/\Delta U^2$ calculated at the midplane is 0.055, 0.027 and 0.022, respectively (the variation is mainly due to the subgrid contribution). Only half the streamwise domain is shown.

2.3. *Subgrid spectra and probability density function*

Hill *et al.* (2006) use the stretched-vortex subgrid model to predict the subgrid part of the two-dimensional radial kinetic (and scalar) energy spectrum tensor for the Richtmyer–Meshkov instability. Here, the expressions for the one-dimensional energy spectrum tensor developed by Pullin & Saffman (1994) are used to calculate the one-dimensional energy spectra. The one-dimensional energy spectrum tensor is defined by

$$\Theta_{ij}(k_3) = \frac{1}{2\pi}\int_{-\infty}^{\infty} R_{ij}(0,0,r_3)\mathrm{e}^{-\mathrm{i}k_3 r_3}\,\mathrm{d}r_3, \tag{2.21}$$

where $R_{ij}(\boldsymbol{r})$ is the velocity correlation $\langle u_i(\boldsymbol{x})u_j(\boldsymbol{x}+\boldsymbol{r})\rangle$. Note that the orientation of the coordinate system used here is arbitrary; hence, the k_3 component of the wave vector $\boldsymbol{k}$ can be aligned in any physical direction. The one-dimensional energy spectrum tensor can also be written as

$$\Theta_{ij}(k_3) = \iint_{-\infty}^{\infty} \Phi_{ij}(\boldsymbol{k})\,\mathrm{d}k_1\,\mathrm{d}k_2, \tag{2.22}$$

where $\Phi_{ij}(\boldsymbol{k})$ is the energy spectrum tensor defined by the Fourier transform pair

$$\Phi_{ij}(\boldsymbol{k}) = \frac{1}{8\pi^3}\iiint_{-\infty}^{\infty} R_{ij}(\boldsymbol{r})\mathrm{e}^{-\mathrm{i}\boldsymbol{k}\cdot\boldsymbol{r}}\,\mathrm{d}r_1\,\mathrm{d}r_2\,\mathrm{d}r_3, \tag{2.23}$$

$$R_{ij}(\boldsymbol{r}) = \iiint_{-\infty}^{\infty} \Phi_{ij}(\boldsymbol{k})\mathrm{e}^{\mathrm{i}\boldsymbol{k}\cdot\boldsymbol{r}}\,\mathrm{d}k_1\,\mathrm{d}k_2\,\mathrm{d}k_3. \tag{2.24}$$

Equation (2.22) shows that there are contributions to the one-dimensional spectrum from all wavenumbers; hence, there will be subgrid contributions to the one-dimensional energy spectrum even when k_3 is in the range of resolvable wavenumbers. For the purposes of calculating this contribution, it is assumed that wavenumbers satisfying $k_1^2 + k_2^2 < k_c^2$ are resolvable (the corner wavenumbers are ignored). For

https://doi.org/10.1017/S002211201000580X Published online by Cambridge University Press

$k_3 < k_c$, the one-dimensional energy spectrum is partitioned as

$$\Theta_{ij}(k_3) = \iint\limits_{k_1^2+k_2^2<k_c^2} \Phi_{ij}(\boldsymbol{k})\,\mathrm{d}k_1\,\mathrm{d}k_2 + \left(\int\limits_{-\infty}^{\infty}\int\limits_{-\infty}^{\infty} \Phi_{ij}(\boldsymbol{k})\,\mathrm{d}k_1\,\mathrm{d}k_2 - \iint\limits_{k_1^2+k_2^2<k_c^2} \Phi_{ij}(\boldsymbol{k})\,\mathrm{d}k_1\,\mathrm{d}k_2 \right). \quad (2.25)$$

The first term, which is subsequently denoted by $\overline{\Theta}_{ij}(k_3)$, is the resolved-scale contribution and is calculated using discrete Fourier transforms of the resolved-scale velocity field to estimate $\Phi_{ij}(\boldsymbol{k})$. The term in brackets, which is subsequently denoted by $\overline{\Theta}_{ij}^{sgs}(k_3)$, is the subgrid contribution and is calculated using the stretched-vortex model to estimate $\Phi_{ij}(\boldsymbol{k})$. General expressions for evaluating the subgrid component for arbitrary vortex orientation distributions are given by Pullin & Saffman (1994), while Chung & Pullin (2009) give expressions for the specific delta function orientation distribution from which the subgrid stress model (2.6) is derived. The only difference here is that it is necessary to take into account the domain of integration in the second term in brackets. The diagonal components of the subgrid one-dimensional energy spectrum tensor are

$$\Theta_{11}^{sgs}(k_3) = \frac{2}{\pi}\left(\frac{I_1 \cos^2\alpha \cos^2\beta + I_2 \sin^2\beta}{\sin\alpha} \right), \quad (2.26)$$

$$\Theta_{22}^{sgs}(k_3) = \frac{2}{\pi}\left(\frac{I_1 \cos^2\alpha \sin^2\beta + I_2 \cos^2\beta}{\sin\alpha} \right), \quad (2.27)$$

$$\Theta_{33}^{sgs}(k_3) = \frac{2}{\pi} I_1 \sin\alpha, \quad (2.28)$$

where α and β are the Euler angles (colatitude and longitude, respectively) of the subgrid vortex relative to the reference frame that is used to define the one-dimensional spectrum (2.21). The quantities I_1 and I_2 are defined by

$$I_1 = \int_0^{s_1} E\left(\frac{\gamma}{s}\right) \left[\frac{1}{s^2} - 1\right]^{1/2} \mathrm{d}s, \quad (2.29)$$

$$I_2 = \int_0^{s_1} E\left(\frac{\gamma}{s}\right) \left[\frac{1}{s^2} - 1\right]^{-1/2} \mathrm{d}s, \quad (2.30)$$

where $E(k)$ is the Lundgren spectrum (2.9) and $\gamma = |k_3/\sin\alpha|$. For $k_3 < k_c$, the subgrid contribution to the resolved scale spectrum $\overline{\Theta}_{ij}^{sgs}(k_3)$ is calculated with $s_1 = \min[1, \gamma/(k_c^2 + k_3^2)^{1/2}]$. For $k_3 > k_c$, there is no resolved contribution to the one-dimensional energy spectrum; hence, the spectrum is calculated from $\Theta_{ij}(k_3) = \Theta_{ij}^{sgs}(k_3)$ with $s_1 = 1$, which is the same as the subgrid-continued spectrum described by Chung & Pullin (2009). The integrals are evaluated using open quadrature formulae.

Subgrid contributions to scalar statistics are also estimated using procedures developed by Hill *et al.* (2006). The subgrid scalar energy is

$$K^c = \int_{k_c}^{\infty} E^c(k)\,\mathrm{d}k, \quad (2.31)$$

where $E^c(k)$ is a model scalar energy spectrum given by

$$E^c(k) = \mathscr{C}\left\{ k^{-5/3} \exp\left(-\frac{4\nu k^2}{3|a|}\right) + \frac{8}{5\pi}\left[\frac{\Gamma}{\pi\nu}\right]^{1/3}\left[\frac{\nu}{|a|}\right]^{1/3} k^{-1} \right\} \exp\left(-\frac{2\mathscr{D}k^2}{3|a|}\right). \quad (2.32)$$

https://doi.org/10.1017/S002211201000580X Published online by Cambridge University Press

The parameter Γ/ν is set to $\Gamma/\nu = 1000$, in accordance with Pullin & Lundgren (2001, § 6C) and Hill *et al.* (2006, § 7.2). In the former work, this value is found to fit experimental data. Note that the coefficient of the second term differs by a factor of $(2\pi)^{1/3}$ to that used by Hill *et al.* (2006), but is consistent with the model developed by Pullin & Lundgren (2001). The parameter $\mathscr{C}$ is calculated from the local spherically averaged second-order scalar structure function $\overline{F}_2^c$ as

$$\mathscr{C} = \frac{\overline{F}_2^c}{A\Delta^{2/3} + B(\nu/|a|)^{1/3}}, \tag{2.33}$$

where A is defined in (2.10) and $B = 4 \times (8/5\pi)(\Gamma/\pi\nu)^{1/3} \int_0^\pi s^{-1}(1 - \sin s/s)\,\mathrm{d}s \approx 9.01726$.

The one-dimensional scalar spectrum is defined by

$$\Theta_{cc}(k_3) = \frac{1}{2\pi} \int_{-\infty}^{\infty} R_{cc}(0, 0, r_3)\mathrm{e}^{-\mathrm{i}k_3 r_3}\,\mathrm{d}r_3, \tag{2.34}$$

where $R_{cc}(\boldsymbol{r})$ is the scalar correlation $\langle c(\boldsymbol{x})c(\boldsymbol{x} + \boldsymbol{r})\rangle$. The one-dimensional scalar spectrum is calculated using procedures analogous to those used for the one-dimensional energy spectrum. The subgrid contribution is given by

$$\Theta_{cc}^{sgs}(k_3) = \frac{2}{\pi}\frac{I_1 + I_2}{\sin\alpha}, \tag{2.35}$$

where I_1 and I_2 are given by (2.29) and (2.30) with $E(k) = E^c(k)$.

The local p.d.f. is estimated using the Beta distribution

$$P_{sgs}(c; \boldsymbol{x}, t) = \frac{\Gamma(a + b)}{\Gamma(a)\Gamma(b)} c^{a-1}(1 - c)^{b-1}, \tag{2.36}$$

where $a(\boldsymbol{x}, t) = \overline{c}\,\phi$, $b(\boldsymbol{x}, t) = (1 - \overline{c})\,\phi$ and $\phi = \overline{c}(1 - \overline{c})/(2K^c) - 1$. The plane-averaged p.d.f. is then calculated from

$$P(c; y, t) = \langle P_{sgs}(c; \boldsymbol{x}, t)\rangle, \tag{2.37}$$

which incorporates contributions from both the resolved and subgrid parts of the scalar field (Hill *et al.* 2006). In the present implementation, discrete approximations of the p.d.f. (histograms) are calculated from the cumulative distribution function given by the incomplete Beta function. The histograms have 32 bins, which is comparable with the number of bins used to collate experimental results. One complication is that the filtered scalar field need not satisfy $0 \leqslant \overline{c} \leqslant 1$ as would a fully resolved scalar field, especially if the effective filter approximates a sharp spectral filter. In practice, this leads to negative values of a and b and $P_{sgs} < 0$. Herein, the values of $\overline{c}$ that are used to calculate the p.d.f. are modified such that $\overline{c} \mapsto 0$ if $\overline{c} < 0$ and $\overline{c} \mapsto 1$ if $\overline{c} > 1$. Scalar excursions of 0.01 or more occupy less than 1 % of the flow domain at $t/\tau = 1900$, with maximum excursions of 0.12. Matheou *et al.* (2010) include a detailed analysis of scalar excursions in a recirculating shear flow using a separate implementation of the stretched-vortex model.

3. Velocity statistics

3.1. *Comparison with experiment*

Case 1A compares favourably with experimental data. Plane-averaged velocity and Reynolds-stress profiles from case 1A are plotted in figures 2 and 3 respectively,

https://doi.org/10.1017/S002211201000580X Published online by Cambridge University Press

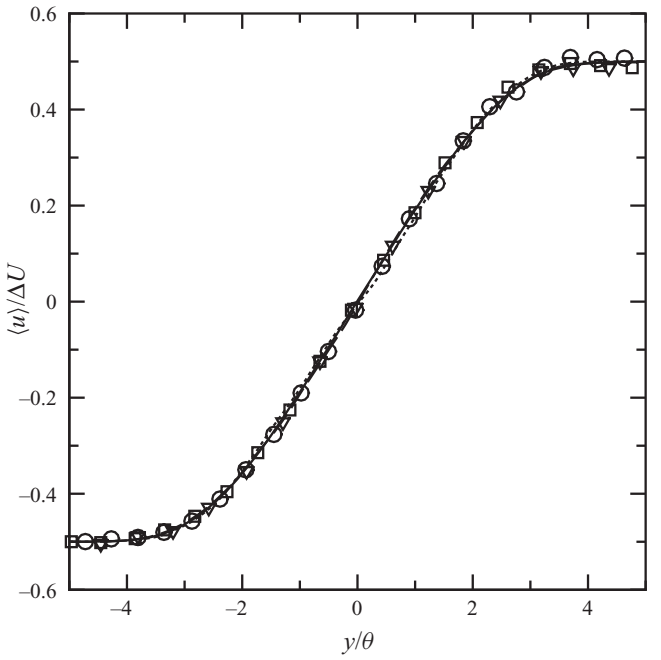


FIGURE 2. Mean velocity profiles at $t/\tau = 416$ (solid line), 800 (long-dashed line) and 1216 (short-dashed line) from case 1A compared with experimental data of Bell & Mehta (1990) at three streamwise positions $x = 108$ cm (squares), 128.4 cm (circles) and 189.4 cm (triangles).

together with the experimental data of Bell & Mehta (1990). These experimental data are from a spatial mixing layer that develops from tripped turbulent splitter-plate boundary layers. The velocity ratio is $U_2/U_1 = 0.6$, where U_2 and U_1 are the low-speed and high-speed fluid velocities, respectively. This appears to be large enough for meaningful comparisons with temporal mixing layers and this dataset has previously been used in that context (Rogers & Moser 1994; Ansari 1997). The maximum Reynolds number achieved in the experiments is approximately 6800, which is comparable with that of the simulation. The Reynolds stress from the simulation is estimated as

$$\langle u_i' u_j' \rangle \approx \langle \overline{u}_i' \overline{u}_j' \rangle + \langle T_{ij} \rangle, \tag{3.1}$$

where $\overline{u}_i' = \overline{u}_i - \langle \overline{u}_i \rangle$ and $u_i' = u_i - \langle u_i \rangle$ (Voekl *et al.* 2000). The mixing layers in the experiment and the simulation each exhibit an interval of linear growth with respect to space and time, respectively. In the simulation, this occurs between $t/\tau = 200$ and 1300 (see figure 4*c*). The data in figures 2 and 3 are plotted at three separate streamwise stations and three separate times during the linear growth phases of the experiment and simulation, respectively. The velocity and Reynolds-stress profiles are self-similar when the cross-stream coordinate is scaled by the momentum thickness. While the flow remains in this self-similar state, there is close agreement between the experimental and simulation data.

There is also close agreement between the growth rate of case 1A and that of the experiment during the linear growth phase. A linear least-squares curve fit to the simulation data during this phase gives a temporal growth rate $r = \mathrm{d}(\theta/\theta_0)/\mathrm{d}(t/\tau) = (1/\Delta U)(\mathrm{d}\theta/\mathrm{d}t) \approx 0.0145$. The correlation coefficient of this fit is 0.9999. The spatial growth rate in the experiment is $\mathrm{d}\theta/\mathrm{d}x = 0.0075$. Assuming

https://doi.org/10.1017/S002211201000580X Published online by Cambridge University Press

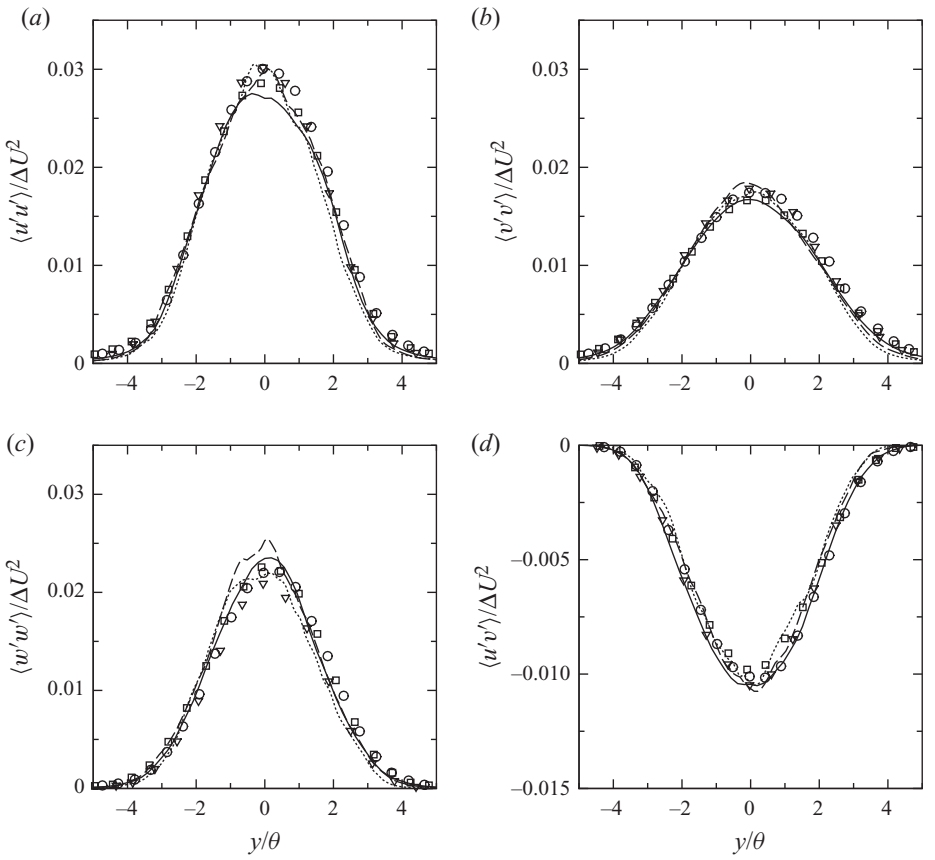


FIGURE 3. (*a–d*) Components of the Reynolds stress tensor from case 1A compared with experimental results (Bell & Mehta 1990). Key as per figure 2.

that spatial derivatives are related to temporal derivatives by $\mathrm{d}/\mathrm{d}t = U_c\,\mathrm{d}/\mathrm{d}x$, where $U_c = \frac{1}{2}(U_1 + U_2)$ is the convection velocity, then the equivalent experimental growth rate is $r = (U_c/\Delta U)(\mathrm{d}\theta/\mathrm{d}x) \approx 0.015$, which is very close to the simulation growth rate. Incidentally, the centreline value of the Reynolds shear stress, $\langle u'v'\rangle(0)/\Delta U^2 \approx -0.0105$, is nearly the same as that obtained from the momentum balance of a self-similar temporal mixing layer, which is related to the growth rate by

$$\frac{\langle u'v'\rangle(0)}{\Delta U^2} = -\frac{1}{\Delta U}\frac{\mathrm{d}\theta}{\mathrm{d}t} \times \int_0^\infty \eta f'(\eta)\,\mathrm{d}\eta \approx -0.0145 \times 0.7071 \approx -0.0103, \qquad (3.2)$$

where $\eta = y/\theta$ and $f(\eta) = \langle u\rangle/\Delta U$ is approximated by an error function. This supports the conclusion that self-similarity has been attained in case 1A.

3.2. *Grid-resolution effects*

Figure 4 shows the integrated turbulent kinetic energy, integrated dissipation rate, momentum thickness and cross-stream velocity variance for cases 1A–1C. These three simulations are identical, except that the grid spacing increases by a factor of two in each respective case (table 1) and cases 1B and 1C are initialised from case 1A at

https://doi.org/10.1017/S002211201000580X Published online by Cambridge University Press

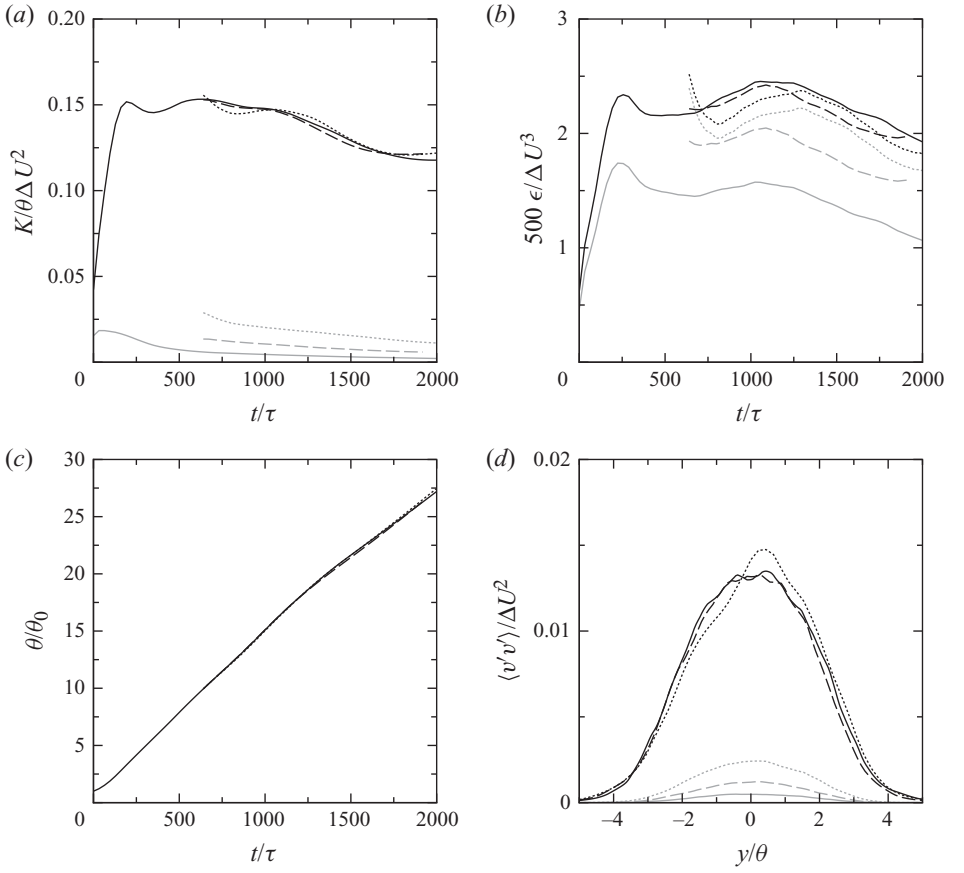


FIGURE 4. Evolution of (*a*) integrated turbulent kinetic energy, (*b*) integrated dissipation, (*c*) momentum thickness and (*d*) a representative turbulence profile at $t/\tau = 1600$ from cases 1A (solid line), 1B (long-dashed line) and 1C (short-dashed line). The light grey curves are the subgrid contributions.

$t/\tau = 640$. The integrated turbulent kinetic energy is

$$\mathscr{K} = \frac{1}{2}\int_{-\infty}^{\infty} \langle u_i'^2 \rangle \, \mathrm{d}y, \tag{3.3}$$

where $\langle u_i'^2 \rangle$ is calculated from (3.1). The integrated dissipation rate is

$$\mathscr{E} = \int_{-\infty}^{\infty} \langle \epsilon \rangle \, \mathrm{d}y, \tag{3.4}$$

where $\epsilon = 2\nu\overline{S}_{ij}\overline{S}_{ij} + \epsilon_{sgs}$. The subgrid dissipation ϵ_{sgs} (more precisely, the rate of energy transfer from large to small scales) is calculated from $\epsilon_{sgs} = -\overline{S}_{ij}T_{ij}$. Figures 4(*a*) and 4(*b*) also show the subgrid contribution to these quantities, $\mathscr{K}_{sgs} = \int_{-\infty}^{\infty}\langle K\rangle \, \mathrm{d}y$ and $\mathscr{E}_{sgs} = \int_{-\infty}^{\infty}\langle \epsilon_{sgs}\rangle \, \mathrm{d}y$. During and after the linear growth phase of case 1A, the subgrid model accounts for as much as 10 % of the total integrated turbulent kinetic energy and about 65 % of the total integrated dissipation. For case 1C, the subgrid model accounts for as much as 20 % of the total integrated turbulent kinetic energy and over 90 % of the total integrated dissipation. In the latter case, the transfer off the grid

https://doi.org/10.1017/S002211201000580X Published online by Cambridge University Press

by the subgrid model dominates the dissipation due to the explicit viscous term in the LES equations, which is important for conclusively testing subgrid models. This is more pronounced for the higher-Reynolds-number simulations, cases 2A–2C. The differences between cases 2A–2C are similar to those between cases 1A–1C; hence, plots of cases 2A–2C are omitted.

The statistics plotted in figure 4 are nearly independent of the grid spacing. Figures 4(*a*) and 4(*b*) show that the subgrid contribution to the integrated turbulent kinetic energy and dissipation increases as the grid spacing is increased in such a way that the total respective values are approximately preserved. The largest excursion occurs for case 1C, in which there is an initial spike in the dissipation that exceeds that of case 1A by about 16 %. This excursion quickly relaxes to less than 10 % and is probably due to a slight incompatibility between the spectral-like filter used to create the initial condition and the subgrid model. The average value of the scaled dissipation rate during the linear growth phase is $500\mathscr{E}/\Delta U^3 \approx 2.3$, which lies between the values of 2.4–2.6 obtained in direct numerical simulations (Rogers & Moser 1994) and the values of 1.5–2 obtained in previous large-eddy simulations (Balaras *et al.* 2001). Figure 4(*c*) shows that the momentum thickness, and hence the growth of the mixing layer, is very accurately preserved as the grid spacing is increased, even though the mixing layer grows by a factor of two. The spatial distributions of the Reynolds stresses are also preserved as the grid spacing is increased. The example shown in figure 4(*d*) is the component of the Reynolds stress tensor with the largest relative subgrid contribution. It is plotted at $t/\tau = 1600$, which allows for significant development of the mixing layer from the initial condition at $t/\tau = 640$. The other components are also nearly independent of the grid spacing and are therefore omitted.

Examples of the resolved and subgrid contributions to the one-dimensional energy spectrum are shown in figure 5. The quantity that is plotted is $E_{ii}(k_x) = 2\Theta_{ii}(k_x)$, which gives $\int_0^\infty E_{ii}(k_x)\,\mathrm{d}k_x = \langle u_i'^2 \rangle$ (Pope 2000). The total resolved-scale spectrum is defined for $k_x < k_c$ and is the sum of the subgrid contribution $\overline{E}_{ii}^{sgs} = 2\overline{\Theta}_{ii}^{sgs}$ and the resolved-scale contribution $\overline{E}_{ii} = 2\overline{\Theta}_{ii}$. The subgrid-continued spectrum is defined for $k_x > k_c$ and consists solely of the subgrid contribution $E_{ii}^{sgs} = 2\Theta_{ii}^{sgs}$. The subgrid contribution to the total resolved-scale spectrum is small but noticeable. The subgrid-continued spectrum only matches the total resolved-scale spectrum when the subgrid contribution to the total resolved-scale spectrum is included. Although not shown here, there is considerable discontinuity between the subgrid-continued spectrum and the total resolved-scale spectrum near the cutoff wavenumber for $t/\tau \lesssim 250$, possibly because the initial resolved-scale and model spectra are incompatible.

One-dimensional spectra from cases 1A–1C and 2A–2C are compared with a model spectrum from Pope (2000) in figure 6(*a*). The high wavenumber part of the model spectrum is

$$\frac{E(k\eta)}{(\epsilon\nu^5)^{1/4}} = \mathscr{K}_0(k\eta)^{-5/3} \exp\left[-\beta\left\{\left((k\eta)^4 + c_\eta^4\right)^{1/4} - c_\eta\right\}\right], \tag{3.5}$$

where $\mathscr{K}_0 = 1.5$, $\beta = 5.2$, $c_\eta = 0.4$ and η is the Kolmogorov length scale $(\nu^3/\epsilon)^{1/4}$. The isotropic relation

$$E_{xx}(k_x) = \int_{k_x}^\infty \frac{E(k)}{k}\left(1 - \frac{k_x^2}{k^2}\right)^{1/2} \mathrm{d}k \tag{3.6}$$

is used to obtain the one-dimensional spectrum from the model. This model spectrum is a close fit to a wide range of experimental spectra (see figure 6.14 in Pope 2000)

https://doi.org/10.1017/S002211201000580X Published online by Cambridge University Press

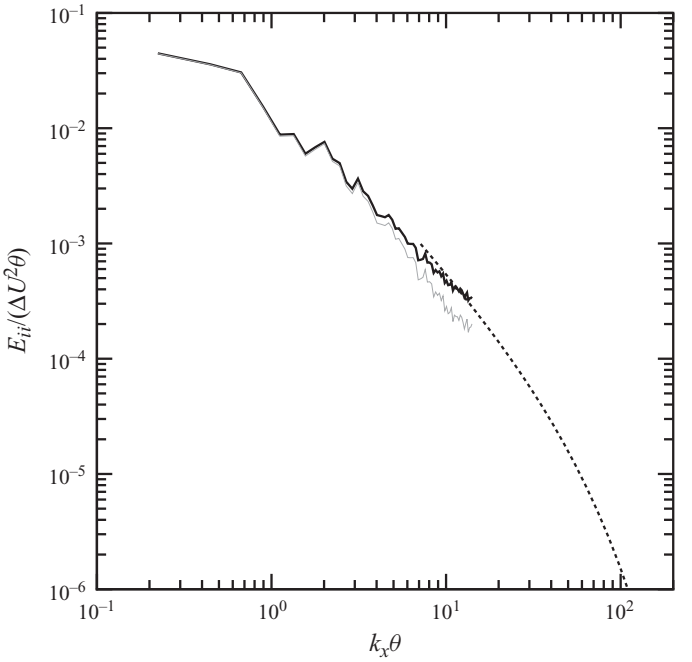


FIGURE 5. One-dimensional energy spectrum at $y=0$ and time $t/\tau=1600$ from case 1C. The solid black line is the total resolved-scale spectrum $E_{ii}=\overline{E}_{ii}+\overline{E}_{ii}^{sgs}$, the solid grey line is the resolved contribution $\overline{E}_{ii}$ and the dashed black line is the subgrid-continued spectrum $E_{ii}=E_{ii}^{sgs}$. In this example, $k_c\theta\approx 14$.

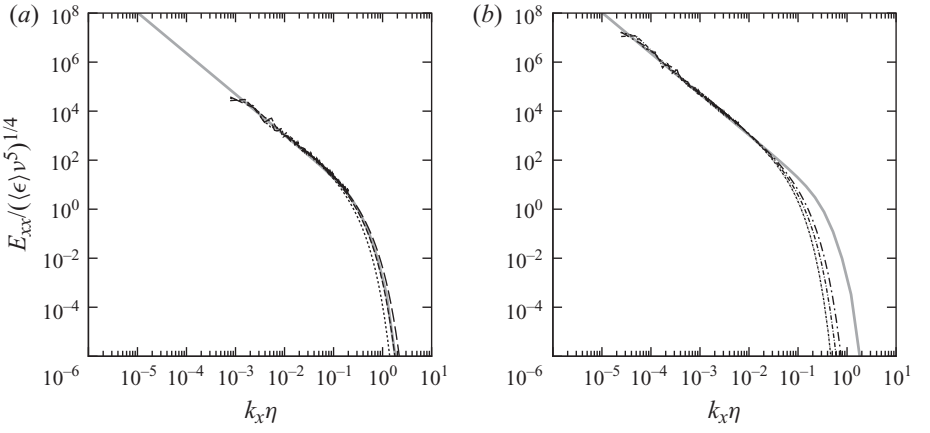


FIGURE 6. Resolved-scale and subgrid-continued one-dimensional energy spectra at $y=0$ and time $t/\tau=1600$ for (*a*) cases 1A (long-dashed line), 1B (medium-dashed line), 1C (short-dashed line) and (*b*) cases 2A (long-dot-dashed line), 2B (medium-dot-dashed line) and 2C (short-dot-dashed line). The solid grey line is the empirical curve fit from Pope (2000).

and is used by Chung & Pullin (2009) to assess spectra from large-eddy simulations of turbulent channel flow. The spectra are normalised by the plane-averaged dissipation $\langle\epsilon\rangle$ and viscosity ν. There is close agreement between the model spectrum (3.5) and the simulation results in the inertial range. However, there is considerable variation

https://doi.org/10.1017/S002211201000580X Published online by Cambridge University Press

between the simulation results in the viscous range. In particular, this figure shows that the viscous cutoff changes from simulation to simulation. Cases 1A–1C differ only in their resolution, as do cases 2A–2C, suggesting that there is some dependence on the grid resolution.

These results are different from those of Chung & Pullin (2009), who found that the subgrid extensions remained unchanged as the grid resolution changed. The present estimate of the subgrid dissipation is different from that used by Chung & Pullin, who calculate it directly from the spectrum of the Lundgren vortex using $\varepsilon_{sgs} = 2\nu \int_{k_c}^{\infty} k^2 E(k)\,\mathrm{d}k$. The close agreement between the model and simulation spectra in the inertial range suggests that the present estimate of $\epsilon_{sgs} = -\overline{S}_{ij} T_{ij}$ is satisfactory. Indeed, if the direct estimate ε_{sgs} is used, it is found that the model (3.5) and simulation spectra do not agree. This is consistent with the spectral deficit in the viscous range, which would tend to decrease the dissipation predicted by $\varepsilon_{sgs} = 2\nu \int_{k_c}^{\infty} k^2 E(k)\,\mathrm{d}k$.

The grid-resolution effect is associated with the scaling of the strain rate a, which is herein estimated from $a = e_i^v e_j^v \overline{S}_{ij}$. The spectrum of the Lundgren vortex (2.9) implies a local viscous length scale $\lambda_\nu \sim (\nu/a)^{1/2}$. The strain rate a is scaled by the local resolved velocity gradient. Based on the model equations (2.10) and (2.11), or dimensional considerations, the local resolved velocity gradient scales as $\epsilon^{1/3}\Delta^{-2/3}$, hence the local viscous length scales as $\lambda_\nu \sim \nu^{1/2}\epsilon^{-1/6}\Delta^{1/3}$. If ϵ is fixed by the large (resolved) scales, this suggests that the viscous length scale will be dependent on the grid spacing for a given flow. Physically, it is expected that λ_ν should follow Kolmogorov scaling, that is, $\lambda_\nu \sim \eta$. However,

$$\frac{\lambda_\nu}{\eta} \sim \frac{\nu^{1/2}\epsilon^{-1/6}\Delta^{1/3}}{\nu^{3/4}\epsilon^{-1/4}} = \left(\frac{\Delta}{\eta}\right)^{1/3}, \tag{3.7}$$

which shows that the disparity between the modelled viscous length scale and the Kolmogorov scale increases the more unresolved the simulation. In wavenumber terms, this is equivalent to $k_\nu \eta \sim (k_c \eta)^{1/3}$, where $k_\nu = 2\pi/\lambda_\nu$ and $k_c = \pi/\Delta$. The scaled wavenumber of the modelled viscous cutoff $k_\nu \eta$ is herein estimated as the wavenumber at which the premultiplied spectrum $(k\eta)^{5/3} E_{xx}(k\eta)/(\epsilon\nu^5)^{1/4}$ falls below 10^{-6}. This is plotted against the scaled grid cutoff wavenumber $k_c\eta$ for cases 1A–1C and 2A–2C in figure 7, which confirms the 1/3 power law.

Chung (2009) finds similar grid-resolution effects on subgrid extensions to spectra from simulations of buoyant mixing flows. He alleviates such problems by estimating $a = (\epsilon/(15\nu))^{1/2}$ and solving for ϵ such that $\epsilon = \overline{S}_{ij}\overline{\tau}_{ij} - \overline{S}_{ij}(\delta_{ij} - e_i^v e_j^v)K(\epsilon)$, where $K(\epsilon)$ is given by (2.8).

4. Scalar mixing

4.1. *Comparison with experiment*

Two examples of the scalar p.d.f. are shown in figure 8. These examples illustrate the two main types of scalar p.d.f.s that are commonly identified in mixing layers. The marching p.d.f. shown in figure 8(*a*) is typical of that from cases 1A–1D and 2A–2C. The non-marching p.d.f. shown in figure 8(*b*) occurs for a limited time during case 4, which is seeded with two-dimensional disturbances. The evolution of case 4 is discussed in § 4.3. The scalar p.d.f. is used to calculate the mixed-fluid fraction

$$p_m(y) = \int_{\varepsilon}^{1-\varepsilon} P(c; y)\,\mathrm{d}c, \tag{4.1}$$

https://doi.org/10.1017/S002211201000580X Published online by Cambridge University Press

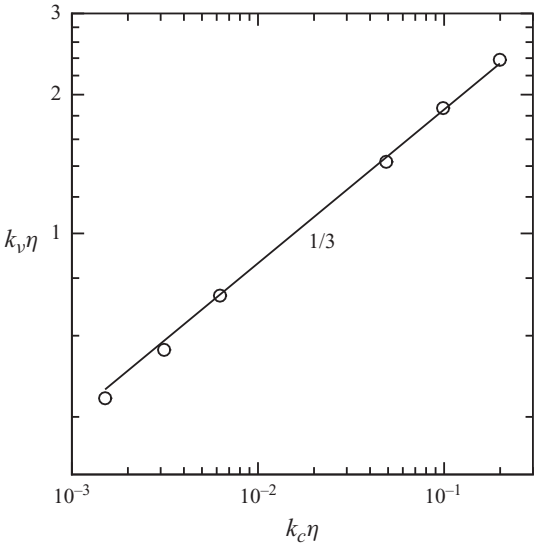


FIGURE 7. Model estimate of the viscous cutoff k_ν as a function of resolution. The solid line has a slope of 1/3.

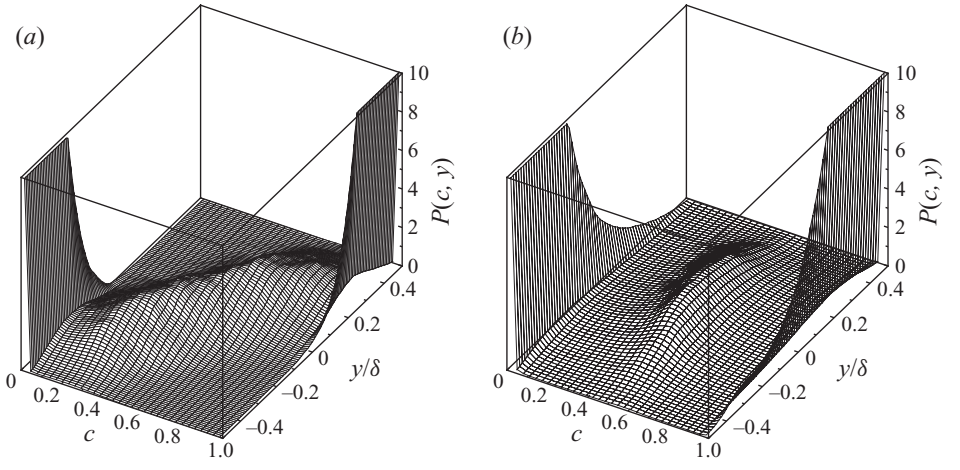


FIGURE 8. Surfaces of the scalar p.d.f. $P(c, y)$ from (*a*) case 1A at time $t/\tau = 1216$ and (*b*) case 4 at time $t/\tau = 416$. The probability axis is clipped at 10.

which is the proportion of fluid in a given plane that is mixed to some degree, and the mixed-fluid composition

$$c_m(y) = \frac{1}{p_m} \int_{\varepsilon}^{1-\varepsilon} c P(c; y)\, \mathrm{d}c, \tag{4.2}$$

which is the average composition of the mixed fluid in a given plane. The small parameter ε distinguishes between mixed and unmixed fluid and is herein set to a value of 1/32, which is consistent with values used in experiments. Measurements of the mixed-fluid fraction and composition are available for both gas and liquid-phase flows, for which the Schmidt numbers are $O(1)$ and $O(1000)$, respectively.

https://doi.org/10.1017/S002211201000580X Published online by Cambridge University Press

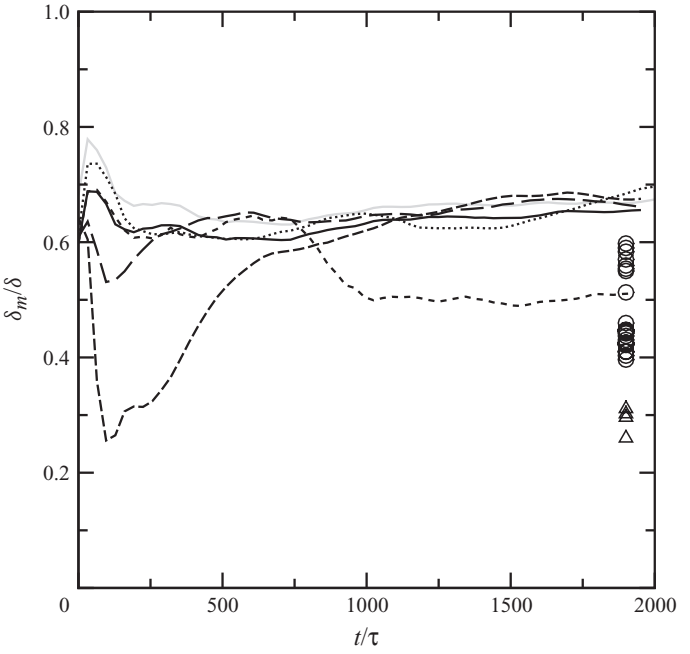


FIGURE 9. Evolution of the mixed-fluid fraction for case 1A (solid black line), case 1D (solid grey line), case 2A (dotted line), case 3 (long-dashed line), case 4 (medium-dashed line) and case 5 (short-dashed line). Circles and triangles denote experimental data for gas-phase flows (Slessor *et al.* 1998; Bond 1999; Meyer *et al.* 2006) at $Re = 30\,000$–$600\,000$ and liquid-phase flows (Koochesfahani & Dimotakis 1986; Karasso & Mungal 1996) at $Re = 14\,000$–$64\,000$, respectively.

The mixed-fluid thickness

$$\delta_m = \int_{-\infty}^{\infty} p_m(y)\,\mathrm{d}y \tag{4.3}$$

is a measure of the total amount of mixed fluid in the layer. The evolution of the total mixed-fluid fraction δ_m/δ is plotted in figure 9. This figure shows the results from several simulations, but here the discussion focuses on those from cases 1A and 1D, which differ only with respect to Schmidt number. During the linear growth phase from $t/\tau = 200$ to 1300, $\delta_m/\delta \approx 0.62 \pm 0.03$ for $Sc = 1000$ (case 1A) and $\delta_m/\delta \approx 0.65 \pm 0.02$ for $Sc = 1$ (case 1D). These values exceed those obtained experimentally. For liquid-phase flows at Reynolds numbers between $Re_\delta = 14\,000$ and 64 000, measured values of the mixed-fluid fraction lie between $\delta_m/\delta = 0.26$ and 0.31 (Koochesfahani & Dimotakis 1986; Karasso & Mungal 1996). For gas-phase flows at Reynolds numbers between $Re_\delta = 30\,000$ and 600 000, measured values of the mixed-fluid fraction lie between $\delta_m/\delta = 0.4$ and 0.6 (see data compiled by Bond 1999, as well as the measurements of Meyer *et al.* 2006). Precise values are weakly dependent on the Reynolds number (Dimotakis 2005) and initial conditions (Slessor *et al.* 1998).

Cross-stream profiles of the mixed-fluid fraction $p_m(y)$ from cases 1A and 1D are plotted in figure 10. In both cases, p_m approaches unity near $y = 0$, indicating that very little unmixed fluid penetrates the midplane. This is consistent with experimental data from gas-phase mixing layers (see the discussion of the gas-phase measurements of Mungal & Dimotakis 1984 in Koochesfahani & Dimotakis 1986 or the gas-phase

https://doi.org/10.1017/S002211201000580X Published online by Cambridge University Press

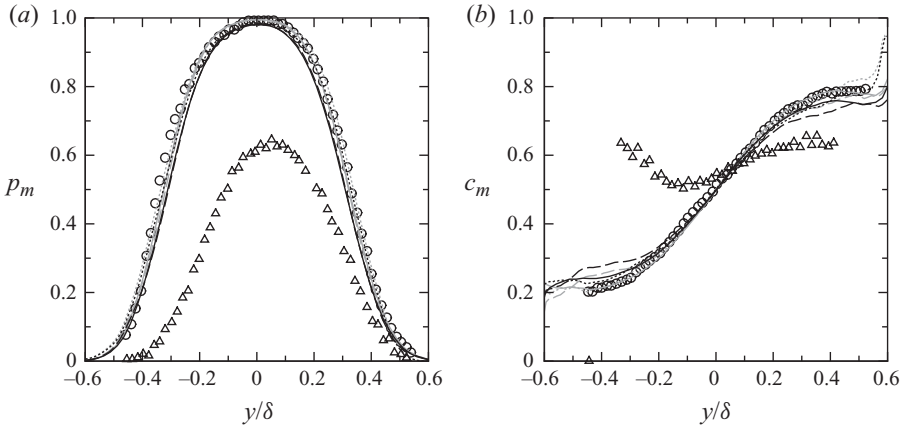


FIGURE 10. Profiles of (*a*) mixed-fluid probability $p_m(y)$ and (*b*) mixed-fluid composition $c_m(y)$ at $t/\tau = 416$ (solid lines), 800 (long-dashed lines) and 1216 (short-dashed lines) from case 1A, $Sc = 1000$ (black) and case 1D, $Sc = 1$ (grey). Symbols are experimental data from liquid-phase experiments at $Re_\delta = 35\,000$ (Karasso & Mungal 1996). Triangles denote fully resolved chemical-reaction data, while circles denote under-resolved passive scalar data.

measurements of Meyer *et al.* 2006), but not with data from liquid-phase mixing layers. In liquid-phase mixing layers, measurements of p_m reach a maximum value of between 0.5 and 0.7 near the midplane (Koochesfahani & Dimotakis 1986; Karasso & Mungal 1996), indicating that significant quantities of unmixed fluid are transported across the layer.

Cross-stream profiles of the mixed-fluid composition $c_m(y)$ from cases 1A and 1D are also plotted in figure 10. In these two cases, the mixed-fluid composition c_m varies considerably across the layer, which indicates that the p.d.f.s have a marching character. This is not consistent with experimental data, especially at high Schmidt number. Measurements in liquid-phase mixing layers show that the variation of the mixed-fluid composition across the layer is weak, which indicates that the p.d.f.s are of the non-marching or 'tilted' type (Koochesfahani & Dimotakis 1986; Karasso & Mungal 1996). The variation of the mixed-fluid composition across a gas-phase mixing layer is larger than that of a liquid-phase mixing layer, but not as large as that observed in the simulations (again, see the analysis of the gas-phase measurements of Mungal & Dimotakis 1984 in Koochesfahani & Dimotakis 1986 or the gas-phase measurements of Meyer *et al.* 2006).

The foregoing comparisons highlight significant differences between the mixed-fluid statistics from cases 1A and 1D and those obtained experimentally, especially at high Schmidt number. The collapse of the mixed-fluid fraction and composition profiles and the invariance of the total mixed-fluid fraction during the linear growth phase indicates that a self-similar state of mixing is achieved. Although the Reynolds numbers of the simulations are reasonably well matched to those of the cited experiments, the maximum velocity ratio of the cited experiments is only $U_2/U_1 = 0.44$, which is even less than that of the dataset used to validate the velocity statistics in § 3.1. It is possible that the disparity between experiment and simulation is due to fundamental differences between spatial and temporal mixing layers. One velocity ratio effect that cannot be captured in a temporal simulation is the preferential entrainment of high-speed fluid into the mixing layer, which affects the average mixed-fluid composition (Dimotakis 1986). On the other hand, Meyer *et al.* (2006) conclude that gas-phase mixing layers

https://doi.org/10.1017/S002211201000580X Published online by Cambridge University Press

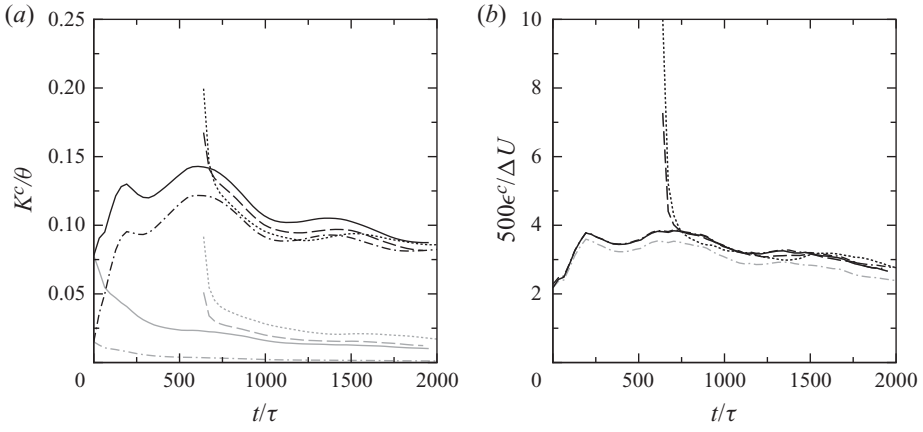


FIGURE 11. Evolution of (*a*) integrated turbulent scalar energy and (*b*) integrated scalar dissipation from cases 1A (solid line), 1B (long-dashed line), 1C (short-dashed line) and 1D (dot-dashed line). The light grey curves are the subgrid contributions.

develop stronger marching characteristics when the velocity ratio is decreased from $U_2/U_1 = 0.44$ to 0.25, which is opposite to the present trend. In liquid-phase mixing layers, the mixed-fluid fraction and the variation of the mixed-fluid composition hardly change when the velocity ratio decreases from $U_2/U_1 = 0.38$ to 0.25 (see figures 12 and 13 in Karasso & Mungal 1996). Indeed, initial conditions (Rogers & Moser 1994; Slessor *et al.* 1998) and the degree of flow development (Karasso & Mungal 1996; Meyer *et al.* 2006) are just as important an influence on the mixed-fluid statistics as the velocity ratio. The effects of initial conditions are explored in § 4.3.

Better agreement is obtained between the mixed-fluid statistics from cases 1A and 1D and under-resolved experimental data. Inadequate resolution has the effect of artificially increasing both the mixed-fluid fraction and the variation of the mixed-fluid composition across the layer (Koochesfahani & Dimotakis 1986; Karasso & Mungal 1996). The under-resolved liquid-phase mixed-fluid data from Karasso & Mungal (1996) plotted in figure 10 are almost indistinguishable from the simulation results. The origin of the cross-stream coordinate of the experimental data is shifted by 0.05 in order to partially accommodate spatial mixing-layer effects (Rogers & Moser 1994). Karasso & Mungal (1996) estimate that this particular dataset is under-resolved by a factor of 1750, based on the effective spatial resolution of the device used to image the flow and an estimate of the Batchelor scale, $\lambda_B = \delta Re_\delta^{-3/4} Sc^{-1/2}$. This is about the same as case 1A, which is under-resolved by a factor of $\Delta/\lambda_B \approx 1780$ when the same estimate of the Batchelor scale is used.

These results support the conjecture that the large-scale structure of the scalar field from cases 1A and 1D is consistent with the experiment of Karasso & Mungal (1996). The magnitude of the subgrid contribution to the scalar p.d.f. is determined by the subgrid scalar energy (2.36), which is itself determined by the model scalar spectrum (2.32). For cases 1A and 1D, the subgrid scalar energy is small relative to the total scalar energy (see figure 11*a*); hence, the subgrid contribution to the scalar p.d.f. is also small. This is the reason why the Schmidt number, which only affects the model subgrid scalar spectrum, has such a weak effect on the mixed-fluid statistics in the simulations (Hill *et al.* 2006). It also means that the total modelled scalar p.d.f. and the derived mixed-fluid statistics are essentially that of the resolved-scale scalar field. As the mixed-fluid statistics are in close agreement with those obtained

https://doi.org/10.1017/S002211201000580X Published online by Cambridge University Press

from under-resolved passive scalar measurements, which are also representative of the large-scale scalar field, it is reasonable to conclude that the large-scale structure of the flow in cases 1A and 1D is comparable with that of the experiment.

4.2. *Grid-resolution effects*

The total integrated scalar energy and scalar dissipation from cases 1A–1D are plotted in figure 11. The total integrated scalar energy is

$$\mathscr{K}^c = \frac{1}{2}\int_{-\infty}^{\infty} \langle c'^2 \rangle \, \mathrm{d}y, \tag{4.4}$$

where $\langle c'^2 \rangle$ is the planar scalar variance

$$\langle c'^2 \rangle \approx \langle \overline{c}'^2 \rangle + 2K^c, \tag{4.5}$$

$\overline{c}' = \overline{c} - \langle \overline{c} \rangle$ and $c' = c - \langle c \rangle$. The total integrated scalar dissipation is given by

$$\mathscr{E}^c = \int_{-\infty}^{\infty} \langle \epsilon^c \rangle \, \mathrm{d}y, \tag{4.6}$$

where $\epsilon^c = \mathscr{D}(\partial \overline{c}/\partial x_j)^2 + \epsilon^c_{sgs}$. The subgrid scalar dissipation is calculated from $\epsilon^c_{sgs} = -q_j \partial \overline{c}/\partial x_j$. Figure 11 also shows the subgrid contribution to these quantities, $\mathscr{K}^c_{sgs} = \int_{-\infty}^{\infty} \langle K^c \rangle \, \mathrm{d}y$ and $\mathscr{E}^c_{sgs} = \int_{-\infty}^{\infty} \langle \epsilon^c_{sgs} \rangle \, \mathrm{d}y$. Figure 11 shows the effects of resolution at a Schmidt number of $Sc = 1000$ (cases 1A–1C), as well as the effect of Schmidt number at fixed resolution (case 1D). In cases 1A and 1D, the initial resolved scalar field is unperturbed, hence the subgrid model initially accounts for almost all the subgrid scalar energy. At later times, the subgrid model accounts for about 20 % of the scalar energy when $Sc = 1000$ and less than 5 % when $Sc = 1$. The subgrid model accounts for almost all the scalar dissipation when $Sc = 1000$ and over 90 % when $Sc = 1$. The total scalar dissipation is about the same regardless of the Schmidt number.

The most prominent features in figures 11(*a*) and 11(*b*) are the large transient spikes in both the scalar energy and the scalar dissipation at the start of the coarse resolution simulations, cases 1B and 1C. The spike in the scalar energy quickly decays to a value that is about 5 %–10 % lower than that of the fine-grid simulation (case 1A), whereas the spike in the scalar dissipation decays to a value that is about the same as that of the fine-grid simulation. In each case, the spike is predominantly due to a disproportionate contribution from the subgrid model as the grid spacing is increased.

One-dimensional scalar spectra from the fine-grid simulation (case 1A) and the coarse-grid simulation (case 1C) are plotted in figure 12. The quantity plotted is $E_{cc}(k_x) = 2\Theta_{cc}(k_x)$, which gives $\int_0^{\infty} E_{cc}(k_x) \, \mathrm{d}k_x = \langle c'^2 \rangle$. As with the velocity spectra, the resolved-scale spectrum includes contributions from the resolved-scale scalar field and the subgrid model. The spectra in figure 12(*a*) are plotted at the start of the coarse-grid simulation; hence, the spectrum for case 1C is the result obtained from the filtered data of case 1A. The spectra in figure 12(*b*) are plotted a short time later, immediately after the transient spikes in the coarse-grid simulation have decayed. Figure 12(*a*) confirms that the filters used to calculate the initial condition for case 1C accurately preserve the initial resolved-scale spectrum. However, the subgrid-continued spectrum of case 1C initially exceeds that of case 1A by a factor of around 2–3. Figure 12(*b*) shows that, shortly afterwards, the high wavenumber modes of the resolved-scale

https://doi.org/10.1017/S002211201000580X Published online by Cambridge University Press

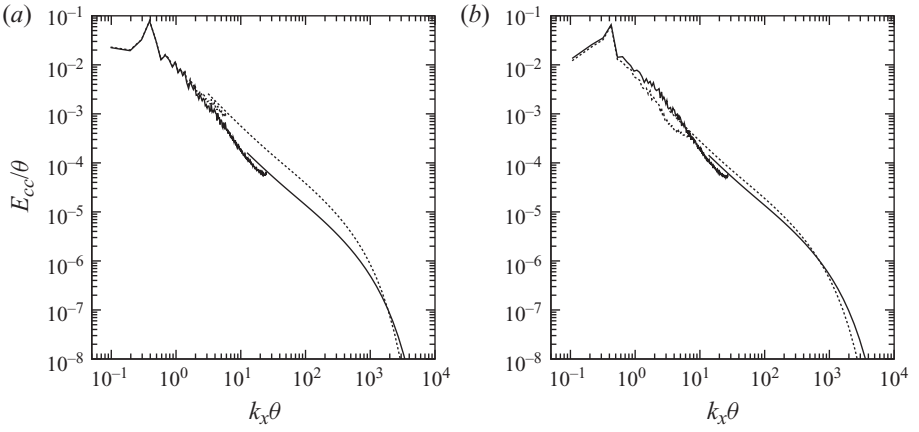


FIGURE 12. One-dimensional scalar spectra at $y = 0$ from cases 1A (solid line) and 1C (dashed line) at times (*a*) $t/\tau = 640$ and (*b*) $t/\tau = 704$. For case 1C at $t/\tau = 640$, $k_c\theta \approx 6$.

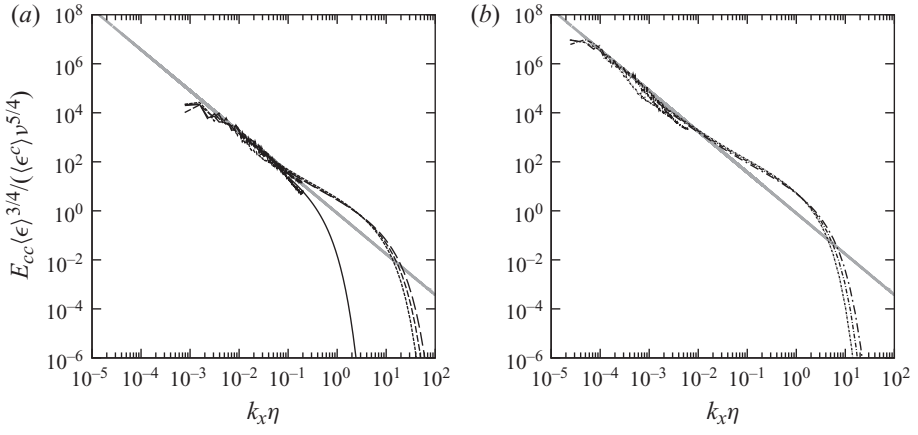


FIGURE 13. Resolved-scale and subgrid-continued one-dimensional energy spectra at $y = 0$ and time $t/\tau = 1600$ for (*a*) cases 1A (long-dashed line), 1B (medium-dashed line), 1C (short-dashed line), 1D (solid line) and (*b*) 2A (long-dot-dashed line), 2B (medium-dot-dashed line) and 2C (short-dot-dashed line). The solid grey line is the power law given by (4.7).

spectrum of case 1C are considerably damped. This allows the subgrid-scale spectrum of case 1C to shift downward, closer to that of case 1A.

It has previously been observed that the scalar flux model is overdissipative at high resolved wavenumbers (Pullin 2000). The spectra in figure 12 confirm that the initial resolved scalar gradients produced by sharp spectral-like filters are indeed excessive for the scalar flux model and are quickly destroyed, temporarily causing a spike in the scalar dissipation. This has the effect of decreasing the magnitude of the resolved second-order scalar structure function and thereby reducing the subgrid scalar energy.

One-dimensional scalar spectra from cases 1A–1D and 2A–2C are plotted using Obhukov–Corrsin scaling in figure 13. In the inertial-convective range, experiments and dimensional arguments suggest that

$$\frac{E_{cc}(k\eta)\epsilon^{3/4}}{\epsilon^c\nu^{5/4}} = \mathscr{C}_0(k\eta)^{-5/3}, \tag{4.7}$$

https://doi.org/10.1017/S002211201000580X Published online by Cambridge University Press

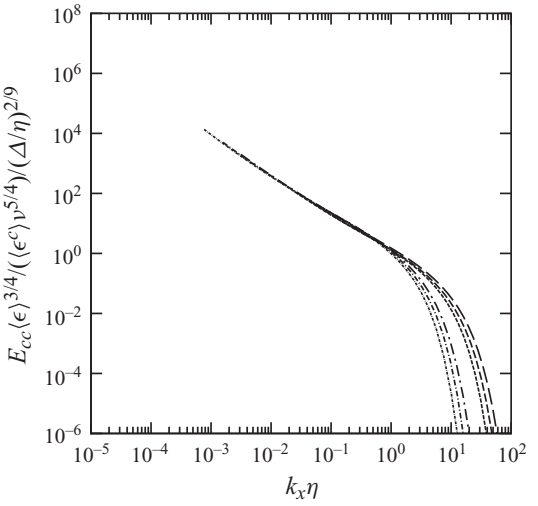


FIGURE 14. Subgrid-continued spectra normalised by $(\Delta/\eta)^{2/9}$. For line styles see figure 13.

where $\mathscr{C}_0 \approx 0.8$ for the present definition of the scalar dissipation (Sreenivasan 1996). This is also plotted in figure 13. The fine-grid simulations, cases 1A, 1D and 2A, each exhibit an inertial-convective range in which the one-dimensional scalar spectrum agrees closely with the empirical spectrum (4.7). However, the spectra from the coarse-grid simulations, cases 1C and 2C, tend to fall below the empirical spectrum, particularly near the grid cutoff wavenumber. As with the velocity spectra, there is considerable variation at high wavenumber. Not only is the diffusive cutoff affected, but there is an upward shift in the k^{-1} contribution to the spectrum when the grid spacing is increased at high Schmidt number, $Sc = 1000$.

These effects are a further consequence of the model assumption $a = e_i^v e_j^v \overline{S}_{ij}$. In non-dimensional form, the subgrid scalar spectrum is

$$\frac{E^c(k\eta)}{\mathscr{C}\epsilon^{-5/12}\nu^{5/4}} = \left\{(k\eta)^{-5/3}\exp\left(-\frac{4}{3}\frac{\lambda_v^2}{\eta^2}(k\eta)^2\right) + \frac{8}{5\pi}\left[\frac{\Gamma}{\pi\nu}\right]^{1/3}\left[\frac{\lambda_v}{\eta}\right]^{2/3}(k\eta)^{-1}\right\} \times \exp\left(-\frac{2}{3}\frac{\lambda_v^2}{\eta^2}\frac{(k\eta)^2}{Sc}\right), \quad (4.8)$$

where $\lambda_v = (\nu/a)^{1/2}$. This implies a diffusive length scale $\lambda_{\mathscr{D}} \sim (\lambda_v/\eta)Sc^{-1/2} \sim (\Delta/\eta)^{1/3}Sc^{-1/2}$. The diffusive length scale retains the conventional dependence on the Schmidt number (cf. the Batchelor scale) but is also dependent on grid resolution, as observed in figure 13. Furthermore, the contribution of the k^{-1} term relative to that of the $k^{-5/3}$ term is increased by a factor of $(\lambda_v/\eta)^{2/3} = (\Delta/\eta)^{2/9}$. Figure 14 shows that the k^{-1} contribution to the scalar spectra collapses when scaled by $(\Delta/\eta)^{2/9}$.

4.3. *Effects of large-scale flow structure*

The last three simulations, i.e. cases 3–5, explore the effect of initial conditions and boundary constraints on the large-scale flow structure and mixed-fluid statistics. Cases 3 and 4 are initialised with perturbations that are elongated in the spanwise direction, whereas case 5 is run in a narrow spanwise domain. Otherwise, the simulations

https://doi.org/10.1017/S002211201000580X Published online by Cambridge University Press

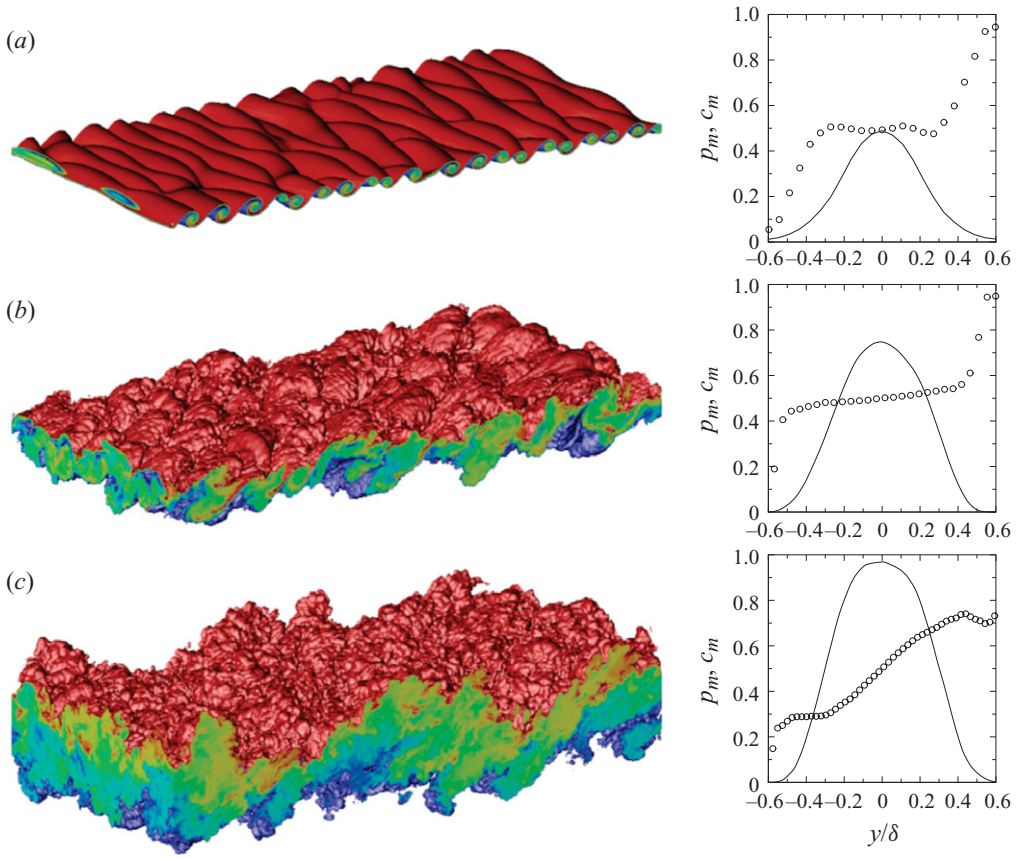


FIGURE 15. (Colour online) Resolved-scale mixed-fluid and mixed-fluid probability (lines) and composition (circles) at (*a*) $t/\tau = 96$, (*b*) 416 and (*c*) 832 from case 4. The shaded surfaces in the visualisations enclose fluid with a resolved composition $\bar{c}$ that is between ε and $1-\varepsilon$, where ε is the same as that used in (4.1).

are identical to case 1A, with a Schmidt number $Sc = 1000$, which approximates liquid-phase mixing.

The evolution of the total mixed-fluid fraction for cases 3–5 is compared with that of case 1A in figure 9. In cases 3 and 4, the total mixed-fluid fraction temporarily decreases to values less than that of case 1A. The decrease is most pronounced in case 4, which reaches values that are consistent with those of liquid-phase mixing-layer experiments. After $t/\tau \approx 100$, the proportion of mixed fluid gradually increases to levels that are roughly similar to those of case 1A. In case 5, the initial evolution of the total mixed-fluid fraction is similar to that of case 1A. Just before $t/\tau \approx 1000$, the mixed-fluid fraction decreases to a value that is significantly less than that of case 1A, although still somewhat higher than that of liquid-phase experiments.

The correlation between the large-scale flow structure and the distribution and composition of mixed fluid for cases 4 and 5 is illustrated in figures 15 and 16, respectively. In case 4, the initial perturbations are seeded at a wavelength that is comparable with that of the most unstable mode. As a result, initial growth is rapid – twice as fast as any other case. The resulting structures are dominated by large-scale spanwise eddies or 'rollers', with very little evidence of an intermediate-scale

https://doi.org/10.1017/S002211201000580X Published online by Cambridge University Press

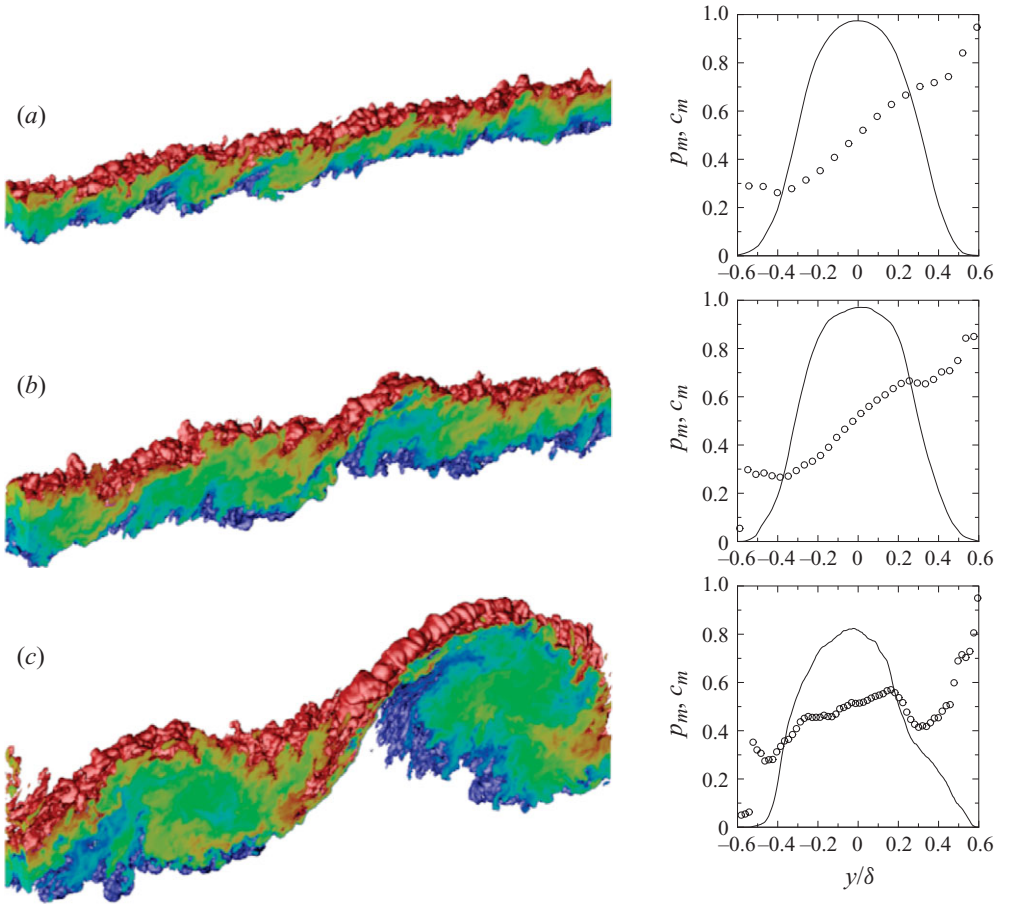


FIGURE 16. (Colour online) Resolved-scale mixed-fluid and mixed-fluid probability (lines) and composition (circles) at (*a*) $t/\tau = 448$, (*b*) 832 and (*c*) 1408 from case 5. Visualisations as in figure 15.

motion (figure 15*a*). As a result, fluid is entrained faster than it is mixed, leading to low values of the mixed-fluid fraction. After $t/\tau = 96$, a kind of 'transition' occurs, with rapid development of disorganised three-dimensional intermediate-scale features and a decrease in the rate of growth. This leads to a steady increase in the mixed-fluid fraction and, for a short time, a flat mixed-fluid composition profile (figure 15*b*), which is consistent with a non-marching p.d.f. (figure 8*b*). The flow subsequently evolves into a state of mixing that is much the same as that of case 1A (figure 15*c*).

The process is essentially reversed in case 5. While the characteristic dimensions of the flow are smaller than, or comparable with, the width of the domain, the resolved-scale flow is three-dimensional and the mixed-fluid statistics are similar to those of case 1A (figure 16*a*). As the flow develops, the growth of spanwise scales is restricted by the narrow domain, while the cross-stream and streamwise scales continue to grow. The growing disparity between these scales leads to the development of a quasi-two-dimensional flow (figure 16*c*). The three-dimensional intermediate-scale structures cannot entrain fluid at the same rate as the larger spanwise eddies, but once the fluid is entrained at the smaller scales it is efficiently mixed. As a result, the proportion of mixed fluid decreases, while the mixed-fluid composition begins to flatten.

https://doi.org/10.1017/S002211201000580X Published online by Cambridge University Press

The foregoing results show that model predictions of the mixed-fluid statistics are more consistent with experiments when the large-scale flow is dominated by spanwise eddies, in accordance with the direct numerical simulations of Rogers & Moser (1994). This can be brought about by promoting two-dimensionality in the initial conditions, as in case 4, or through boundary constraints, as in case 5. However, in the present simulations, the stimulation needed to produce an effect of sufficient magnitude is rather strong. In case 3, for example, elongation of the initial perturbations in the spanwise direction is insufficient to produce a state of mixing that is substantially different from that of case 1A. It is only when the fundamental instability is specifically excited in case 4 that the initial growth of the spanwise eddies is sufficiently fast to produce the necessary effect. Periodic spanwise boundary constraints only exert a significant influence on the mixed-fluid statistics when the thickness of the mixing layer is considerably larger than the span of the domain.

There is no evidence of distinct self-similar states of mixing arising from cases 3 and 4. In both cases, the mixed-fluid statistics eventually approach values that are comparable with those of the self-similar state obtained in case 1A. In case 4, the growth rate continues to evolve throughout the simulation and a self-similar state is never attained. In case 3, there is a period of linear growth between $t/\tau = 500$ and 1000, during which the growth rate is $r = 0.0123$ (cf. case 1A, for which $r = 0.0145$), while the relevant statistics collapse at least as well as they do for case 1A (these statistics are omitted). However, the mixing layer grows only by a factor of 2 during the period of linear growth in case 3, compared with a factor of 5.5 in case 1A. Although this is comparable with the growth obtained during the self-similar phase of other mixing-layer simulations (e.g. Rogers & Moser 1994; Balaras *et al.* 2001), it only accommodates one complete vortex amalgamation, which may not be sufficient to be sure that a distinct self-similar state has in fact been achieved. If a distinct self-similar state has been achieved in case 3, its state of mixing is not significantly different from that of case 1A.

5. Conclusions

The stretched-vortex subgrid model has been used to run large-eddy simulations of temporal mixing layers at Reynolds and Schmidt numbers that are comparable with those attained in experiments. Model predictions of velocity and scalar statistics have been compared with experimental data for a range of initial conditions and boundary constraints.

Random plane-isotropic perturbations produce a flow that is self-similar for a limited time (cases 1A and 1D). During the self-similar growth phase, the mean velocity, Reynolds stress and growth rate compare favourably with experiment. These statistics, as well as the turbulent kinetic energy and dissipation rate, are not sensitive to moderate changes in the grid resolution. However, grid resolution decreases the wavenumber of the viscous cutoff in the subgrid-continued energy spectrum. This is due to the assumption that the appropriate strain rate in the model subgrid spectrum (2.9) is that of the resolved-scale velocity field. This has little effect on the velocity statistics because it only affects the subgrid contribution to the turbulent kinetic energy, which is much smaller than the resolved-scale contribution.

There are, however, significant differences between the mixed-fluid statistics obtained from cases 1A and 1D and those obtained experimentally. In particular, the simulations overpredict both the amount of mixed fluid in the layer and the variation of the mixed-fluid composition across the layer. This is most significant at

https://doi.org/10.1017/S002211201000580X Published online by Cambridge University Press

high Schmidt number. Better agreement is obtained when the large-scale structure of the flow is quasi-two-dimensional, which is achieved by elongating the initial perturbations in the spanwise direction (cases 3 and 4) or by decreasing the spanwise width of the domain (case 5). However, the degree of two-dimensionality needed to produce the necessary effect is strong and could not be sustained.

It is suggested that the resolved-scale structure of the scalar field from cases 1A and 1D is actually in accord with the experiment because the mixed-fluid statistics from cases 1A and 1D (which are largely unaffected by subgrid contributions and therefore representative of the resolved-scale scalar field) closely match *under-resolved* experimental data (which are also representative of the large-scale scalar field). If this is so, then the discrepancies in the mixed-fluid statistics must be attributed to model estimates of the subgrid scalar p.d.f. Several factors have been identified in this paper that might affect subgrid scalar model fidelity. These include the dissipation of intermediate-scale features by the subgrid flux model as well as the dependence of the subgrid scalar spectrum on the grid resolution, both of which affect the subgrid scalar variance or energy and, in turn, the subgrid scalar p.d.f. The assumed Beta distribution, which is used to estimate the subgrid scalar p.d.f., also has limitations. Although the Beta distribution can model a bimodal distribution of unmixed fluid (with peaks at $c = 0$ and 1), it cannot model a bimodal distribution with peaks centred on other values of c (say, at $c = 0$ and 0.5). This might be relevant near the edges of the layer where fluid that has been thoroughly mixed finds itself remixed with fresh fluid.

REFERENCES

Ansari, A. 1997 Self-similarity and mixing characteristics of turbulent mixing layers starting from laminar initial conditions. *Phys. Fluids* **9**, 1714–1728.

Balaras, E., Piomelli, U. & Wallace, J. M. 2001 Self-similar states in turbulent mixing layers. *J. Fluid Mech.* **446**, 1–24.

Bell, J. H. & Mehta, R. D. 1990 Development of a two-stream mixing layer from tripped and untripped boundary layers. *AIAA J.* **28**, 2034–2042.

Blaisdell, G. A., Spyropoulos, E. T. & Qin, J. H. 1996 The effect of the formulation of nonlinear terms on aliasing errors in spectral methods. *Appl. Numer. Maths* **21**, 207–219.

Bond, C. L. 1999 Reynolds number effects on mixing in the turbulent shear layer. Master's thesis, California Institute of Technology.

Chung, D. 2009 Numerical simulation and subgrid-scale modeling of mixing and wall-bounded turbulent flows. PhD thesis, California Institute of Technology.

Chung, D. & Pullin, D. I. 2009 Large-eddy simulation and wall modelling of turbulent channel flow. *J. Fluid Mech.* **631**, 281–309.

Dimotakis, P. E. 1986 Two-dimensional shear-layer entrainment. *AIAA J.* **24**, 1791–1796.

Dimotakis, P. E. 1991 Turbulent free shear layer mixing and combustion. In *High Speed Flight Propulsion Systems* (ed. S. N. B. Murthy & E. T. Curran). *Progress in Astronautics and Aeronautics*, vol. 137, pp. 265–340. AIAA.

Dimotakis, P. E. 2005 Turbulent mixing. *Annu. Rev. Fluid Mech.* **37**, 329–356.

Druault, P., Lardeau, S., Bonnet, J.-P., Coiffet, F., Delville, J., Lamballais, E., Largeau, J. F. & Perret, L. 2004 Generation of three-dimensional turbulent inlet conditions for large-eddy simulation. *AIAA J.* **42**, 447–456.

Faddy, J. M. & Pullin, D. I. 2005 Flow structure in a model of aircraft trailing vortices. *Phys. Fluids* **17**, 085106.

Ghosal, S. 1996 An analysis of numerical errors in large-eddy simulations of turbulence. *J. Comput. Phys.* **125**, 187–206.

Hill, D. J., Pantano, C. & Pullin, D. I. 2006 Large-eddy simulation and multiscale modelling of a Richtmyer–Meshkov instability with reshock. *J. Fluid Mech.* **557**, 29–61.

https://doi.org/10.1017/S002211201000580X Published online by Cambridge University Press

Hill, D. J. & Pullin, D. I. 2004 Hybrid tuned center-difference–WENO method for large eddy simulations in the presence of strong shocks. *J. Comput. Phys.* **194**, 435–450.

Huang, L. S. & Ho, C. M. 1990 Small-scale transition in a plane mixing layer. *J. Fluid Mech.* **210**, 475–500.

Karasso, P. S. & Mungal, M. G. 1996 Scalar mixing and reaction in plane liquid shear layers. *J. Fluid Mech.* **323**, 23–63.

Koochesfahani, M. M. & Dimotakis, P. E. 1986 Mixing and chemical reactions in a turbulent liquid mixing layer. *J. Fluid Mech.* **170**, 83–112.

Kosovic, B., Pullin, D. I. & Samtaney, R. 2002 Subgrid-scale modeling for large-eddy simulations of compressible turbulence. *Phys. Fluids* **14**, 1511–1522.

Kravchenko, A. G. & Moin, P. 1997 On the effect of numerical errors in large eddy simulations of turbulent flows. *J. Comput. Phys.* **131**, 310–322.

Lele, S. K. 1992 Compact finite difference schemes with spectral-like resolution. *J. Comput. Phys.* **103**, 16–42.

Lesieur, M. & Metais, O. 1996 New trends in large-eddy simulations of turbulence. *Annu. Rev. Fluid Mech.* **28**, 45–82.

Matheou, G., Bonanos, A. M., Pantano, C. & Dimotakis, P. E. 2010 Large-eddy simulation of mixing in a recirculating shear flow. *J. Fluid Mech.* **646**, 375–414.

Mattner, T. W., Pullin, D. I. & Dimotakis, P. E. 2004 Large eddy simulations of miscible Rayleigh–Taylor instability. In *9th International Workshop on the Physics of Compressible Turbulent Mixing, Cambridge, UK*.

Meneveau, C. & Katz, J. 2000 Scale-invariance and turbulence models for large-eddy simulation. *Annu. Rev. Fluid Mech.* **32**, 1–32.

Meyer, T. R., Dutton, J. C. & Lucht, R. P. 2006 Coherent structures and turbulent molecular mixing in gaseous planar shear layers. *J. Fluid Mech.* **558**, 179–205.

Michalke, A. 1964 On the inviscid instability of the hyperbolic-tangent velocity profile. *J. Fluid Mech.* **19**, 543–556.

Misra, A. & Pullin, D. I. 1997 A vortex-based subgrid stress model for large-eddy simulation. *Phys. Fluids* **9**, 2443–2454.

Mungal, M. G. & Dimotakis, P. E. 1984 Mixing and combustion with low heat release in a turbulent shear layer. *J. Fluid Mech.* **148**, 349–382.

Pantano, C., Pullin, D. I., Dimotakis, P. E. & Matheou, G. 2008 LES approach for high Reynolds number wall-bounded flows with application to turbulent channel flow. *J. Comput. Phys.* **227**, 9271–9291.

Pope, S. B. 2000 *Turbulent Flows*. Cambridge University Press.

Pullin, D. I. 2000 A vortex-based model for the subgrid flux of a passive scalar. *Phys. Fluids* **12**, 2311–2319.

Pullin, D. I. & Lundgren, T. S. 2001 Axial motion and scalar transport in stretched spiral vortices. *Phys. Fluids* **13**, 2553–2563.

Pullin, D. I. & Saffman, P. G. 1994 Reynolds stresses and one-dimensional spectra for a vortex model of homogeneous anisotropic turbulence. *Phys. Fluids* **6**, 1787–1796.

Rogers, M. M. & Moser, R. D. 1994 Direct simulation of a self-similar turbulent mixing layer. *Phys. Fluids* **6**, 903–923.

Slessor, M. D., Bond, C. L. & Dimotakis, P. E. 1998 Turbulent shear-layer mixing at high Reynolds numbers: effects of inflow conditions. *J. Fluid Mech.* **376**, 115–138.

Sreenivasan, K. R. 1996 The passive scalar spectrum and the Obukhov–Corrsin constant. *Phys. Fluids* **8**, 189–196.

Stuart, J. T. 1967 On finite amplitude oscillations in mixing layers. *J. Fluid Mech.* **29**, 417–440.

Voekl, T., Pullin, D. I. & Chan, D. C. 2000 A physical-space version of the stretched-vortex subgrid-stress model for large-eddy simulation. *Phys. Fluids* **12**, 1810–1825.

Vreman, B., Geurts, B. & Kuerten, H. 1997 Large-eddy simulation of the turbulent mixing layer. *J. Fluid Mech.* **339**, 357–390.

https://doi.org/10.1017/S002211201000580X Published online by Cambridge University Press